UNIVERSITY OF PÉCS

Doctoral School of Physics

Pump pulse width and temperature effects in high energy lithium niobate THz sources

PhD Thesis

Csaba Lombosi

Supervisor
Dr. József András Fülöp
senior research scientist

Supervisor
Dr. János Hebling
full professor

PÉCS, 2017

Contents

List of symbols and conventions

LN	lithium niobate
EO	electro-optic
EOS	electro-optic sampling
EOC	electro-optic crystal
TPFP	tilted-pulse-front pumping
RT	room temperature
CT	cryogenic temperature
IR	infrared
ps	picosecond
fs	femtosecond
c_0	speed of light in vacuum
ω_i	frequencies at optical spectral range
λ_i	wavelengths at optical spectral range
Ω_i	frequencies at THz spectral range
ϵ_0	vacuum permittivity
μ_0	vacuum permeability
k	wavenumber
Δk	phase mismatch
γ	pulse front tilt angle
P_L	linear polarization
P_{NL}	nonlinear polarization
FT	Fourier transformation
FL	Fourier limited

Preface

My research activities aim at the improvement of single-cycle terahertz source conversion efficiency by experimentally confirming results of theoretical works: optimization of pump pulse duration and temperature for lithium niobate (LN, $LiNbO_3$) based terahertz sources. Also, I would like to enhance the knowledge of beam properties of terahertz radiation source with μJ-level energy, so that developing new applications could benefit from it.

I have completed my studies at the Institute of Physics, Faculty of Sciences, University of Pécs (Hungary). However, experiments were also conducted abroad, thanks to collaborations with international groups at Max Planck Institute of Quantum Optics (Munich, Germany), Amplitude Systems (Pessac, France), and Paul Scherrer Institute (Villigen, Switzerland). Although I wrote my thesis in first person singular, shown results are a product of team effort.

Chapter 1

Introduction

Intense terahertz source development in the last decade allowed the growth of new areas of research. Tilted-pulse-front pumping [1] of inorganic $LiNbO_3$ (LN) shows good characteristics to achieve the highest possible pulse energies below 1 THz [2-5]. Ultrafast carrier dynamics of semiconductors were measured by THz pump - THz probe measurements [6], molecule alignment with an intense field [7] and electron wave streaking [8] were also demonstrated. THz-assisted attosecond pulse generation [9], would also benefit from intense terahertz pulses. The above mentioned applications require peak electric fields on the order of 100 kV/cm. However, newly emerging areas as acceleration, longitudinal compression, and undulation of relativistic electron bunches [10-12], post-acceleration of laser-generated proton and ion beams with potential applications for hadron therapy [13], multispectral single-shot imaging, THz-enhanced attosecond-pulse generation with increased cut-off frequency [9] would benefit from field strengths higher than currently provided. Multi-mJ and multi-10-MV/cm level sources are needed for these applications.

Today extremely high field strengths up to 100 MV/cm are available only in the frequency range above 10 THz [14]. Although the mentioned applications would highly benefit from low frequency THz sources, so that longer wavelength is preferably matching typical transversal sizes of particle beams, pulse energies and peak electric fields

necessary for these applications is presently not available. Therefore, it is a priority to optimize THz pulses generated by optical rectification of fs laser pulses with tilted-pulse-front pumping in lithium niobate [1]. Theoretical studies [15-17] predict an increase in efficiency with optimization of pump pulse duration and cryogenic cooling of LN source crystal.

Chapter 2

Theoretical background

Generation of far-infrared radiation in electro-optical crystals and characterization of such sources were realized in the early 1970's [18,19]. Although generation of near single-cycle pulses in the terahertz region began in the 1980's [20], efficiency was far from optimal. Nowadays, development of terahertz radiation has a growing interest for new applications where the highest possible THz energies are needed. Consequently, there is a need for the development of efficient, high-field THz sources. Scaling of THz sources has its limitations. High intensity THz sources rely on nonlinear frequency conversion of optical laser pulses. Thus, scaling relies highly on optimization of pump-to-THz generation efficiency. THz pulses can be generated with many different techniques. The most promising technique is optical rectification of ultrashort laser pulses in LN. Other techniques generating THz pulses in the few-THz frequency range involving organic crystals are also hopeful [21-24]. However, my thesis concentrates on the lower frequency spectrum, which has an advantage in particle beam manipulation owing to the larger wavelengths ($\lambda > 300$ μm).

2.1 Optical rectification of ultrashort laser pulses

In this Section I give a brief theoretical description on THz generation by optical rectification of ultrashort laser pulses. Common knowledge mentioned in this Section is covered in detail in [25-35]. I will focus on phase-matching geometry with tilted-pulse-front scheme, since that was used throughout my experiments.

Interaction between light and matter occurs e.g. when bound electrons in materials respond to electromagnetic (EM) waves. The altered electron distribution produces charge separation andthe matter becomes polarized. Induced polarization P(t) is proportional to its triggering EM wave's E(t) electric field

$$P(t) = \epsilon_0 \chi^{(1)} E(t), \tag{2.1}$$

where ϵ_0 is vacuum permittivity, and $\chi^{(1)}$ is the linear susceptibility. As driving electric field gets stronger we should use power series expansion of the polarization to calculate polarization, and higher order components should be taken into account

$$\begin{aligned} P(t) &= \epsilon_0 \left[\chi^{(1)} E(t) + \chi^{(2)} E^2(t) + \dots \right] = \\ &= P^{(1)}(t) + P^{(2)}(t) + \cdots = \\ &= P_L(t) + P_{NL}(t) \end{aligned} \tag{2.2}$$

where the new components are the higher-order susceptibility and polarization components, respectively. Polarization can be separated to two distinct parts, $P_L(t)$ and $P_{NL}(t)$ corresponding to linear and nonlinear polarization, respectively.

Let us have two different pump lasers with ω_1 and ω_2 frequencies, respectively, which are propagating inside a dispersive medium at a speed of $c_i = c_0/(n(\omega_i))$ where n(ω_i) is the refractive index of the medium at ω_i frequency. Considering nonlinear polarization terms only to the second order one can observe many phenomena. For the two lasers

let's consider

$$E_1(t) = E_1 \exp(-i\omega_1 t) + c.c., \tag{2.3}$$

$$E_2(t) = E_2 \exp(-i\omega_2 t) + c.c., \tag{2.4}$$

than as the two lasers interact in the media the polarization induced through the nonlinear polarization effects can be expressed as

$$P_{NL}(t) = \epsilon_0 \chi^{(2)} \left[2E_1 E_2 \exp -i(\omega_1 + \omega_2) t + E_1^2 \exp -i\omega_1 t + E_2^2 \exp -i\omega_2 t \right.$$
$$\left. + 2E_1 E_2^x \exp -i(\omega_1 - \omega_2) t + c.c. \right] + 2\epsilon_0 \chi^{(2)} \left[E_1 E_1^x + E_2 E_2^x \right]$$

where the first term is responsible for sum-frequency generation (SFG), the second and third term describes the second harmonic generation (SHG) that is a special case of SFG, the fourth term describes the different frequency generation (DFG) and the last term is optical rectification (OR). Optical rectification is a special case of second order nonlinear polarization effects, and is very similar to difference frequency generation (DFG). Phase matching condition determines which effect will occur. Commonly, an infrared (IR) laser is used for generating THz pulses, so let us take an IR photon with frequency ω_1, and another photon close to the former frequency with a frequency of ω_2. These can mix together and generate a photon at their difference frequency, $\omega_1 - \omega_2 = \Omega$. The frequency of this photon lies within the THz range. To understand optical rectification in THz generation, one can consider it as an intrapulse DFG (as shown in Figure 2.1), where mixing takes place between frequency components of the same broadband, ultrashort laser pulse. It is worth noting that down-conversion of the ω_1 photon can happen multiple times. This repeated process is called cascading, and it can occur in cycles, because difference between ω_1 and $\omega_1 - \Omega$ is so small that phase-matching condition is still fulfilled. Cascading effect can be detected as the IR

pump pulse will be redshifted and broadened after THz generation.

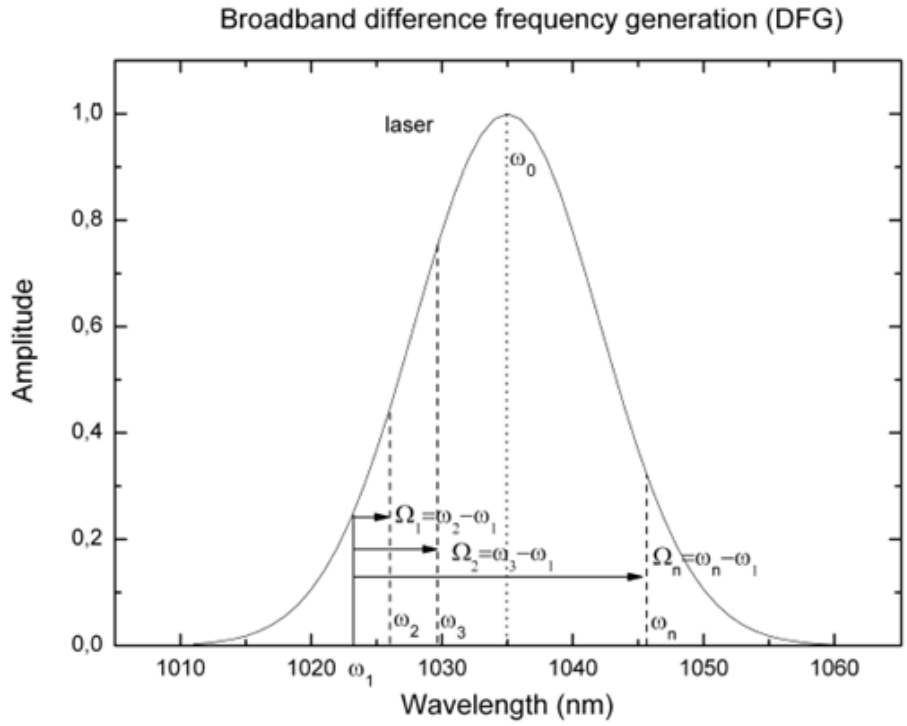

Figure 2.1: Intrapulse difference frequency generation

One-dimensional frequency domain wave equation of the generated field can be derived from Maxwell's equations for a THz pulse at Ω central frequency as follows

$$\frac{\partial E\left(\Omega,z\right)}{\partial z^2}+k^2\left(\Omega\right)E\left(\Omega,z\right)=\frac{\Omega^2}{\epsilon_0 c_0^2}P_{NL}\left(\Omega,z\right) \tag{2.5}$$

where direction of propagation is parallel to the wavevector k, and the corresponding wavenumber is $|k|=\Omega\frac{n(\omega)}{c_0}$ inside the source medium. Evolution of the complex amplitude E(Ω,z) of the generated THz field can be given by using the slowly varying envelope approximation, considering the absorption along z-direction, as

$$\frac{\partial E\left(\Omega,z\right)}{\partial z^2}=-\frac{1}{2}\alpha\left(\Omega\right)E(\Omega,z)-\frac{i\mu_0\Omega c_0}{2n(\omega)}P_{NL}\left(\Omega,z\right)\exp\left[-i\Delta kz\right] \tag{2.6}$$

where the first term corresponds to the THz loss due to material absorption, that contains the absorption coefficient $\alpha(\Omega)$. The second term corresponds to the gain due

to the nonlinear polarization, μ_0 is the vacuum permeability, and $P_{NL}(\Omega, z)$ can be expressed as

$$P_{NL}(\Omega, z) = \epsilon_0 \chi^{(2)}_{eff} \int_0^\infty A(\omega + \Omega) A^*(\omega) d\omega \tag{2.7}$$

where $\chi^{(2)}_{eff}$ is the second order nonlinear susceptibility coefficient, A(ω) is the complex amplitude of the generating electric field. In Equation 2.6 $\Delta k = k_{\omega_1+\Omega} - k_{\omega_1} - k_\Omega$ is the phase mismatch. At each point of the second-order polarization oscillation it emits radiation, that are interfering constructively with each other only if the wavevectors of the generating components and the new (terahertz) component are in a phase-matching condition: $k_\Omega = k_{\omega_1} - k_{(\omega_1-\Omega)}$.

For a plane wave and perfect phase matching (Δk=0) Equation 2.6 can be solved to determine the efficiency of the generation

$$\eta = \frac{2\Omega^2 d_{eff}^2 L^2 I}{\epsilon_0 n_g \left(\omega\right)^2 n(\Omega) c_0^3} \exp\left[-\alpha(\Omega)\frac{L}{2}\right] \frac{\sinh\left[\alpha(\Omega)\frac{L}{4}\right]}{\left[\alpha(\Omega)\frac{L}{4}\right]^2} \tag{2.8}$$

where d_{eff} is the effective nonlinear coefficient, L is the interaction length, n_g is the group refractive index, and I is the intensity of the pumping laser. For large absorption ($\alpha(\Omega) \cdot L >> 1$) Equation 2.8 gives

$$\eta \propto \frac{8 I d_{eff}^2 \Omega^2}{\epsilon_0 n_g(\omega)^2 n(\Omega) c_0^3 \alpha(\Omega)^2} \tag{2.9}$$

Equation 2.9 shows that the efficiency of the optical rectification is proportional to the pump pulse intensity, the square of effective nonlinear coefficient, the square of the THz frequency, and inversely proportional to the square of the THz absorption coefficient. Also, I have to note that Equations 2.9 gives only an upper limit on efficiency. With the help of 2.9 we can determine whether a nonlinear material is proper for efficient THz generation. One can characterize a specific crystal's aptitude to operate as an efficient THz source through the figure-of-merit (FOM), that is derived from the previous equation

$$FOM = \frac{4 d_{eff}^2}{n(\omega)^2 n(\Omega) \alpha(\Omega)^2} \tag{2.10}$$

In the frequency range above 10 THz optical rectification can be achieved by using GaSe crystal, where the shorter wavelength makes it easier to tightly focus the generated beam and achieve electric fields above 100 MV/cm [14]. High-frequency, intense THz sources can also be built by using DAST organic crystal, where achievable electric fields are around hundreds of kV/cm [21,36]. Using DAST the available electric field makes possible that one can easily perform pump-probe measurements.

At lower frequencies, a promising material for generating intense THz pulses is zinc

material	λ(nm)	d_{eff} (pm / V)	n_g	n_{THz}	α_{THz} (cm^{-1})	FOM
GaSe	1060	28.0	3.13[37]	3.72[38]	0.07[39]	5300
ZnTe	800	68.5	3.31[40]	3.17[41]	1.3[41]	106
$LiNbO_3$	1060	168	2.23[42]	5.16[43]	16[43]	4.6

Table 2.1: Properties of common materials used for THz generation [44]

material	λ = 1064 nm		λ = 1560 nm	
	pump absorption	tilt angle(°)	pump absorption	tilt angle(°)
GaSe	2PA	25.9	3PA	30.2
ZnTe	2PA	22.4	3PA	28.6
$LiNbO_3$	4PA	63.4	5PA	63.8

Table 2.2: Pump pulse absorption and needed tilting angle for phase-matching at different materials. 2PA, 3PA, 4PA, 5PA corresponds to two-photon, three-photon, four-photon, and five-photon absorptions.

telluride. Promising pulse energies up to 1.5 μJ was demonstrated by Blanchard et al. [45]. However, generation efficiency is limited because the phase-matching condition is fulfilled at the optical frequency near the band gap of zinc telluride (2.26 eV). Thus, generation is saturated due to free carriers generated by two-photon absorption. To overcome this limiting factor, semiconductor based sources can be pumped above the three-photon absorption edge. Polónyi et al. has successfully generated THz pulses with 14 μJ energy with an efficiency as high as 0.7%, while using a pump pulse at 1.7 μm wavelength [46].

Another promising nonlinear material for terahertz generation is lithium niobate crystal, with a large band-gap and large second-order nonlinear susceptibility, even though collinear configuration cannot satisfy phase-matching conditions since the difference between group refractive index in the near infrared ($n_g \approx 2.2$) and phase refractive index in the THz frequency region (n$\approx$ 5.2) is not negligible [47]. It has been demonstrated that one can generate THz radiation based on Cherenkov radiation [20,48], and broadband THz pulses can be generated by a LN waveguide prism [49,50].

Although one could say that mentioned semiconductors would be a better match for terahertz generation, however considering pump absorption and necessary pulse tilting for phase match shown in Table 2.2. proves that LN is good choice. For pumping at

1064 nm GaSe and ZnTe need a smaller angle of pulse-tilt, but tow-photon absorption of the pump occurs which limits the usable maximum intensity. In case of LN at the same wavelength only four-photon absorption occurs, though one needs larger pulse-tilting that affects also imaging properties, too.

2.2 Tilted-pulse-front pumping

Section 2.1 has covered key aspects of optical rectification and collinear phase matching, and their limitations in lithium niobate. To overcome these limitations an important step is to solve noncollinear phase matching [51,52] in order to achieve high conversion efficiency. This section covers the tilted-pulse-front pumping (TPFP) technique to resolve the problem. For difference frequency generation the phase mismatch Δk can be written as

$$\begin{aligned} \Delta k(\Omega) &= k(\Omega) + k(\omega_1) - k(\omega_1 + \Omega) \\ &\cong k(\Omega) - \Omega \left.\frac{dk}{d\omega}\right|_{\omega_1} \\ &\cong \frac{\Omega}{c_0}\left[n(\Omega) - n_g(\omega_1)\right] \end{aligned} \tag{2.11}$$

where ω_1 is the central frequency of the pumping laser, and I used the approximation $\omega_1 \gg \Omega$. Equation 2.11 shows that Δk is proportional to the difference of the phase refractive index at generated THz radiation frequency and of the group refractive index at driving laser frequency. Having lithium niobate as a source crystal the difference between these key parameters would result in a short coherence length

$$L_{coh} = \frac{\pi}{\Delta k} = 0.77mm \tag{2.12}$$

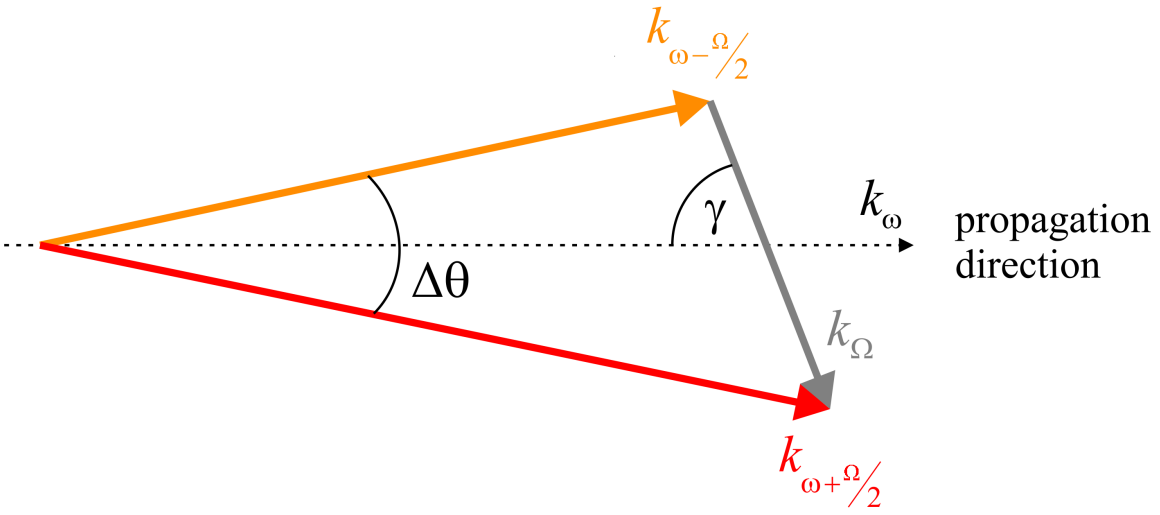

Figure 2.2: Phase-matching relation illustrated by wavevector conservation [1].

that makes efficient THz generation impossible. Phase-matching techniques like quasi-phase-matching [53-55] make it possible to increase the coherence length, although they have some limitation factors as smaller effective coefficient (d_{eff}), and multi-cycle terahertz generation. In order to minimize phase mismatch in a noncollinear geometry one can apply the tilted-pulse-front pumping technique.

Figure 2.2 illustrates wave-vector conservation. This scheme makes the matching of velocities possible. The beam propagating in the z-direction is tilted by an angle of γ with respect to the propagation direction. One can calculate this angle by

$$\cos\gamma = \frac{n_g(\omega_1)}{n(\Omega)} \tag{2.13}$$

Modifying phase mismatch coordinates by a coordinate transform of $z^I = z/\cos\gamma$ gives

$$\Delta k \cong \frac{\Omega}{c_0}\left[n(\Omega) - \frac{n_g(\omega_1)}{\cos\gamma}\right] = 0 \tag{2.14}$$

From Equation 2.14 one can see that the pulse tilted by the right angle satisfies the phase matching condition and the velocity vector of the pumping beam's pulse front coincides with the velocity vector of the generated THz pulse.

Angular dispersion leads to pulse front tilt. The corresponding tilt angle can be

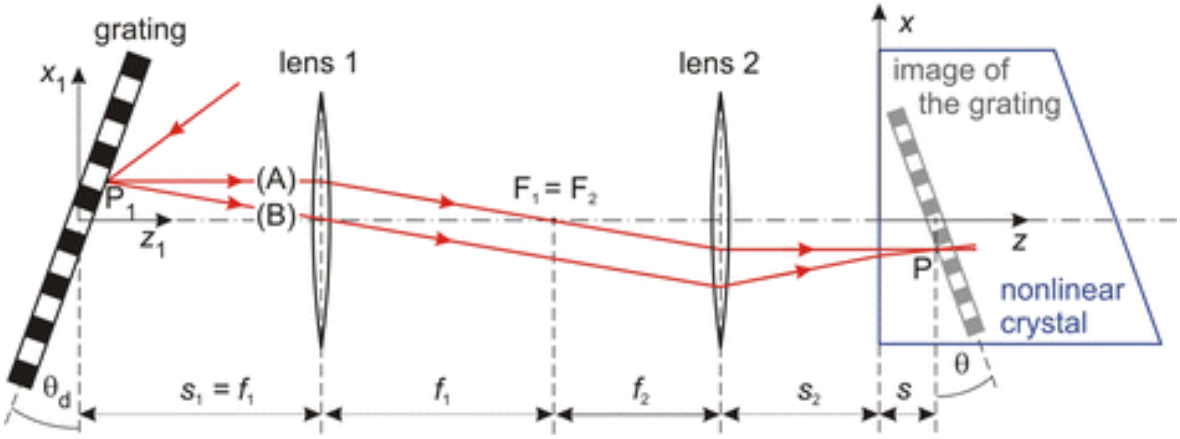

Figure 2.3: Realization of the Tilted-pulse-front pumping scheme, and its key parameters [15].

expressed in terms of angular dispersion as

$$\tan\gamma = \frac{n(\omega_1)}{n_g(\omega_1)}\lambda\frac{d\theta}{d\lambda} \tag{2.15}$$

where λ is a wavelength corresponding to a ω frequency. Figure 2.3 shows a design concept of a high intensity terahertz source using tilted-pulse-front pumping scheme. Tilting is realized by a reflection type blazed grating, and a pair of lenses is used to image the tilted-pulse-front into the crystal.

2.3 Detection of terahertz pulses

An indispensable part of experiments is characterization. The following Section covers briefly power, beam profile and temporal profile measurement techniques.

2.3.1 Power and beam profile measurement of THz beams

To measure pulse power in the mm and sub-mm wavelength range one can use bolometers and pyroelectric detectors. Usually, thermal detectors have an absorbing surface or volume with a known heat capacity, which converts the incident radiation to heat. The absorber is connected to a heatsink to reach equilibrium with room temperature when

the absorber is not irradiated. The temperature change in the absorber is detected and converted to an electronic signal with a temperature sensitive resistance. These types of detectors are often used so that it gives a periodic response and a calibration curve is used to calculate the irradiated power [56].

Bolometers The bolometer that was developed by Langley [57] is a thermal detector, that consist of a resistance thermometer and a radiation absorber. This technique is wildly used by many applicants, as the absorber material can easily be changed to optimize the equipment for any given spectral range. After a long journey of the bolometers, the modernization began by Boyle and Rogers [58] where low temperature carbon radio resistors were used. Today's bolometers are either metal bolometers working at room temperature, or semiconductor based structures operated at cryogenic temperature, enabling better sensitivity. Compared to conventional detectors, efficiency and sensitivity is much higher, although they are very slow, due to the need to return to thermal equilibrium at every irradiation period.

Pyroelectric sensors A pyroelectric or polar crystal, is a spontaneously polarized crystal where each unit cell has a permanent electric dipole moment aligned with a specific crystal axis. The spontaneous electric polarization is sensitive to changes in the temperature, thus the name pyroelectricity. An often-used material for pyroelectric detectors is lithium tantalite ($LiTaO_3$).

Although surface charge accompanies the spontaneous polarization, it is neutralized by free carriers. This charge balance is the important point of the detection. The crystal is sandwiched between two electrodes [59] as Figure 2.4 shows and altogether they form a capacitor. Usually the top electrode also acts as the radiation absorber. As irradiation raises the temperature of the pyroelectric crystal reduces the spontaneous polarization as well as surface charge and whenever the circuit closes, current will flow through the capacitor. Real-time circuits are somewhat more complicated. Figure 2.5

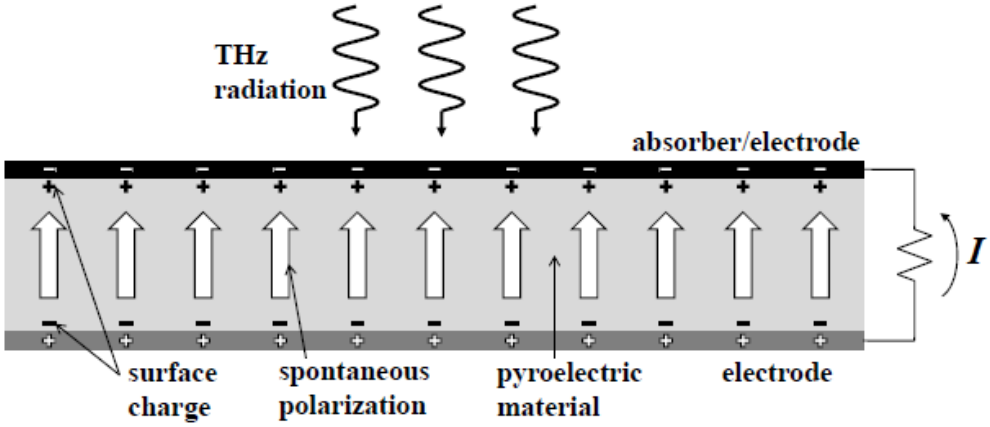

Figure 2.4: Schematic diagram of a typical pyroelectric detector [35].

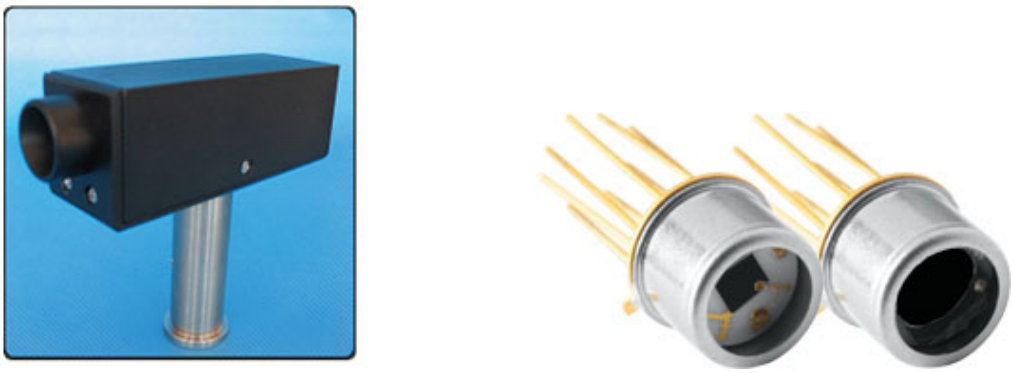

Figure 2.5: Microtech $LiTaO_3$ detector (left), and Gentec QS9-THz-BL detector (right).

shows the two detectors that I used for my measurements.

Beam profiler Along with power measurement, spectroscopic sensing, 2D THz imaging was realized by time-domain spectroscopy with raster scanning of chemical samples. Unfortunately, this method needs long acquisition times, thus making real-time imaging impossible. Many research groups began development of real-time cameras [60] by microbolometer arrays. Since microbolometers require thermal isolation structures with typical time-constants of many milliseconds, illumination has to be done with high duty cycle sources. Also, this technique is matched to a higher frequency range (1.5 to 100 THz).

Another technique to measure 2D beam profiles is modern pyroelectric array cameras

that can operate at room temperatures. The camera usually consists of a $LiTaO_3$ crystal, just as mentioned in the *Pyroelectric sensors* part, mounted to a readout multiplexer electronic part. As IR light illuminates the pyroelectric crystal, it is absorbed and converted to heat. This creates surface charges that can be detected by the multiplexer array and can easily be converted into a 2D picture. During the readout the camera electronics can generate a very short electronic shutter to record the thermally generated signal with a better signal-to-noise ratio. Figure 2.6 shows the Spiricon Pyrocam III pyroelectric camera that was used during experiments.

Figure 2.6: Spiricon Pyrocam III for IR beam profiling [Ophir Optronics].

2.3.2 Measurement of time dependent electric field

To detect terahertz pulses two methods are commonly used today in the lower THz frequency range: photoconductive (PC) antenna detection, and free-space electro-optic sampling, both in synchronous, and asynchronous optical sampling mode. Detection of THz pulses with the PC method is analogous to the generation process: a fs laser with a photon energy larger than the semiconductors bandgap is focused on the semiconductor (low-temperature-grown GaAs, LT-GaAs [35]) target and generates free carriers.

Whenever a THz pulse reaches the target within the lifetime of the generated carriers, they will be accelerated in the direction of the THz electric field and collide with the electrodes that are placed on the target substrate. This will generate a small, but measurable current up to tens of nano-amperes. Usually, on top of the semiconductor plate there is a hemispheric Si lens, directly attached to the substrate, so the THz beam can be coupled efficiently into the semiconductor.

A limiting factor of the PC detection is the rise time of the photocurrent, that is influenced by the material properties of the antenna's semiconductor substrate itself. Another important time factor is the pulse length of the fs laser pulse

$$J(t) \propto \int N(t) \cdot E_{THz}(t) dt \tag{2.16}$$

Fourier transformation of Equation 2.16 gives

$$J(\omega) \propto \int N(\omega) \cdot E_{\omega} dt \tag{2.17}$$

where J(ω) is the measured current density, N(ω) is the carrier concentration in the target substrate and its rise time is also determined by the gating, which in this case is the fs laser pulse [61-63].

Another method for time dependent electric field measurement is the electro-optic sampling (EOS). The detection relies on the Pockels effect that is the birefringence of a crystal in external electric field. As the THz pulse is much longer ($\approx$ 2 ps) than the probing pulse ($\approx$ 100 fs) from the probe beam's perspective THz radiation is a DC field. The effect is the inverse effect to the optical rectification, and can be written as

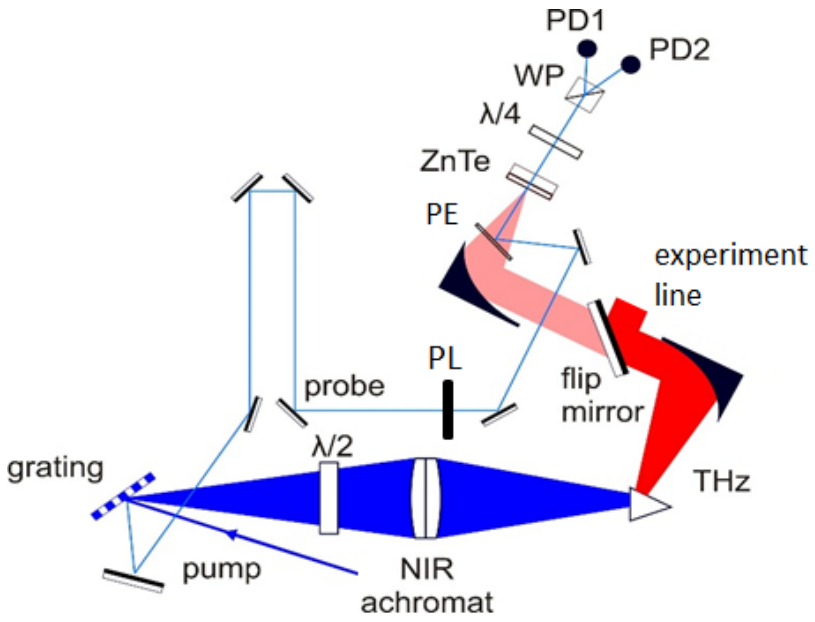

Figure 2.7: Schematic drawing of a THz source and EOS setup, blue color shows the pump and probe beam while red color shows the generated THz source.

$$P_i^{(2)}(\omega) = 2\sum_{j,k} \epsilon_0 \chi i, j, k^{(2)}(\omega.\omega, 0) E_j(\omega) E_k(\omega) \tag{2.18}$$
$$= \sum_j \epsilon_0 \chi_{i,j}^{(2)}(\omega) E_j(\omega)$$

where $\chi_{ij}^{(2)}$ is the field-induced susceptibility. Equation 2.18 shows that the induced polarization is proportional to the THz electric field that induces it, and thus recorded electric field is, too.

Most common semiconductors used for EOS are GaP and ZnTe. Usually, a fraction of the source pumping beam is used as probing beam and the external field is the THz pulse [64,65]. The Pockels effect occurs only when the two beams coincide both spatially and temporally. The upper part of Figure 2.7 shows a schematic of the EOS system. The setup consists of a polarizer (PL), a pellicle beam combiner (PE), a zinc telluride electro-optic crystal (ZnTe), a quarter-wave retardation plate ($\lambda/4$), a

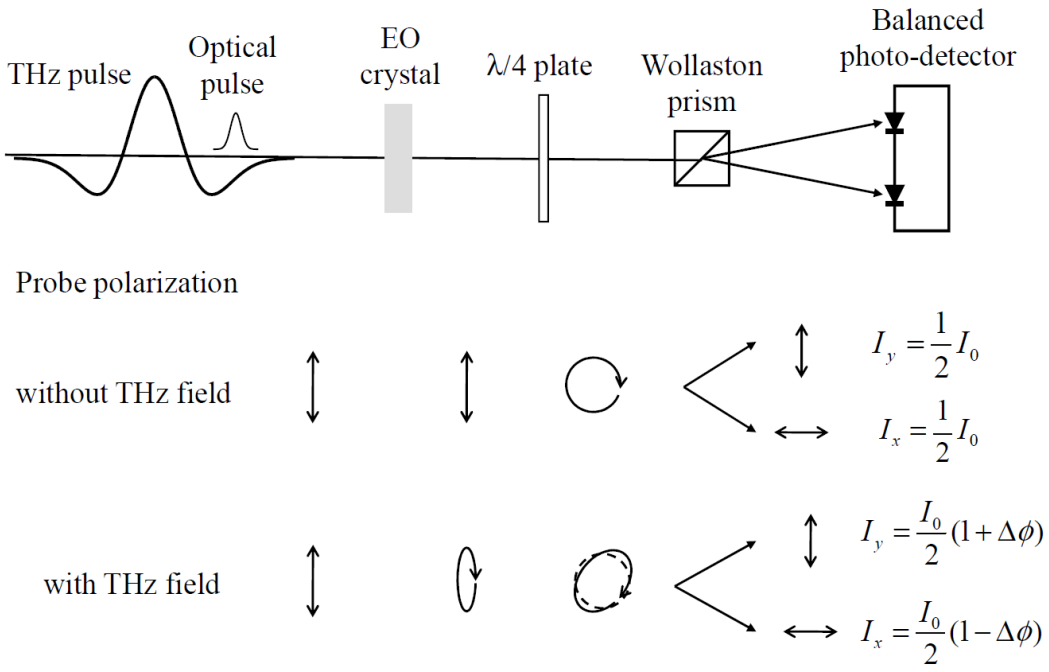

Figure 2.8: Polarization state change of the probe beam along the EOS setup, with and without external THz field.

polarizing beam splitter e.g. Wollaston-prism (WP), and two balanced detectors (PD1 and PD2).

The electro-optic mechanism works as follows:

(i) **Without the THz field** (Figure 2.8), a linearly polarized probe propagates through the EO crystal without any change. After the quarter–wave plate the polarization changes to circular. The Wollaston prism divides the beam to the two orthogonal polarizations. At the end, the balanced photo-detectors record the same intensities. Thus, there is no THz signal recorded.

(ii) While the EO crystal senses **the THz field** (Figure 2.8), the field will induce a temporal birefringence. As the linearly polarized probe propagates through the EO crystal – in case the probe pulse and THz pulse overlap in time – it becomes slightly elliptically polarized. After the quarter-wave plate, the altered beam advances into a nearly circularly polarized state. The prism divides the beam, as in (i). At the end, the detectors will receive two different intensities.

The measured difference, $I_s = I_y - I_x$ between the two recorded components is proportional to the amplitude of the external THz field at the exact time of the overlap.

To maximize the signal detection sensitivity, one should maximize the induced birefringence. This is achieved by rotating the $\langle 110 \rangle$ oriented EO crystal's $\left[1\bar{1}0\right]$ axis parallel to the inducing field, and the optical polarization's axis [66]. The nonlinear polarization at the probe beam's frequency is orthogonal to the incident optical field, thus the differential phase retardation $\Delta\phi$ that effects the probe beam can be written as

$$\Delta\phi = (n_y - n_x)\frac{\omega L}{c_0} = \frac{\omega L}{c_0} n_O^3 r_{41} E_{THz} \tag{2.19}$$

where n_O is the refractive index at the probe's ω frequency, r_{41} is the EO coefficient, and L is the distance over witch the Pockels effect is present. Intensities seen by the balanced photodetectors are affected by $\Delta\phi$

$$I_x = \frac{I_0}{2}(1 - \sin\Delta\phi) \approx \frac{I_0}{2}(1 - \Delta\phi), \tag{2.20}$$

$$I_x = \frac{I_0}{2}(1 - \sin\Delta\phi) \approx \frac{I_0}{2}(1 - \Delta\phi), \tag{2.21}$$

where I_0 is the probe beam intensity before separation. Approximation is only true for small ($\Delta\phi \ll 1$) differential phase retardation. The criterion is also necessary to properly measure time dependent THz electric field, considering that the signal of the photo-detectors is proportional to the THz field amplitude

$$I_s = I_x - I_y = I_0\Delta\phi = \frac{I_0\omega L}{c_0} n_O^3 r_{41} E_{THz} \propto E_{THz} \tag{2.22}$$

By sweeping the probe pulse through the different points of the THz pulse we can scan the entire time dependent electric field. With this technique not only temporal envelope, but also phase information can be retrieved. Thus, complex dielectric constant of materials can be calculated. While free-space electro optic sampling method is a

robust scheme, it has its limitations, especially when detecting ultra-broadband THz pulses. Limitations are as follows: (i) pulse duration of optical probe, (ii) wavelength dependence of nonlinear coefficient, and (iii) mismatch between optical group velocity and THz phase velocity. The detector's response function H combines these limitation factor, and the EO signal is a convolution of the THz field with H

$$E_s(t) = E_{THz} * H(t) \tag{2.23}$$

that can be written in the following form as well

$$E_s(\Omega) = E_{THz}(\Omega) \cdot H(\omega, \Omega). \tag{2.24}$$

Equation 2.24 gives a simple correlation between the electric field and the response function in the frequency domain. H(ω, Ω) is a product of the three limiting factors

$$H(\omega, \Omega) = A_{Opt}(\Omega) \cdot \chi^{(2)}(\omega; \Omega, \omega - \Omega) \cdot \Delta\phi(\omega, \Omega) \tag{2.25}$$

where $\chi^2\,(\omega; \Omega, \omega - \Omega)$ is the second-order nonlinear coefficient, $\Delta\phi\,(\omega, \Omega)$ is the frequency-dependent phase retardation due to velocity mismatch and $A_{Opt}\,(\Omega)$ is the autocorrelation function that can be written as

$$A_{Opt}(\Omega) = \int_{-\infty}^{\infty} E^*_{Opt}(\omega^I - \omega) E_{Opt}(\omega^I - \omega - \Omega) d\omega^I \tag{2.26}$$

Figure 2.9 shows the $H\,(\omega, \Omega)$ response function between 0 and 5 THz for ZnTe, 100 fs pulse duration, calculated for several crystal thicknesses. For ZnTe the main limiting factor is the phase mismatch. It reduces highly the detection bandwidth while increasing the crystal thickness. Also, effects due to absorption will rise with thicker crystals.

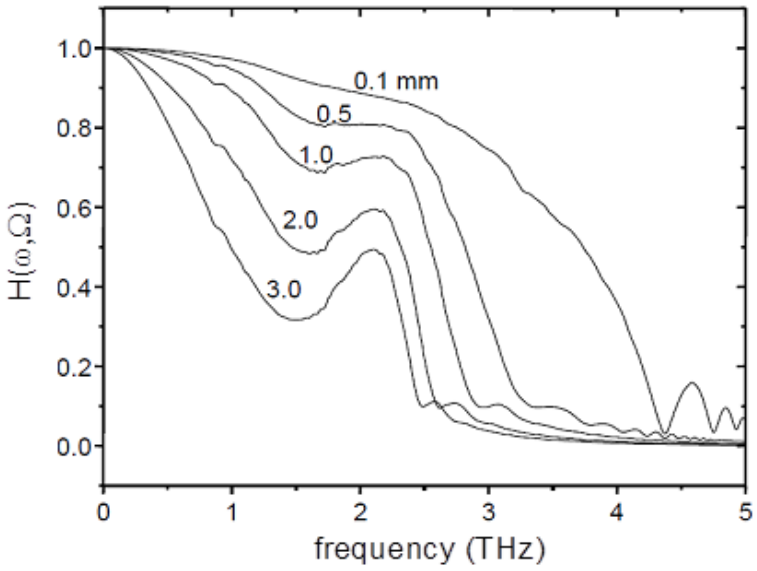

Figure 2.9: Normalized detector function of a commonly used semiconductor, ZnTe, for a few crystal thicknesses, when optical pulse duration is 100 fs [35].

Chapter 3

Scientific goals

Extremely high field strengths up to 100 MV/cm are currently available only in the frequency range above 10 THz. Evolving areas as acceleration and undulation of relativistic electron bunches, acceleration of laser-generated proton and ion beams would benefit from low frequency THz sources, so that longer wavelength is preferably matching typical transversal sizes of particle beams. Thus, improvement is needed in THz pulse energies and peak electric fields for these applications.
My goal is to experimentally prove results of theoretical studies that predict improvement of single-cycle terahertz source conversion efficiency:

(i) Study THz generation pumped by a laser source that emits transform-limited pulses between 0.38 ps and 0.65 ps with pulse energies up to 15 mJ at 1030 nm central wavelength and find the optimal pump pulse duration.

(ii) Study THz generation in cooled lithium niobate sources and show the enhancement factor that can be reached by cooling the source crystal for sources up to $45\mu J$ THz pulse energy and for sources between $50\mu J$ and about $180\mu J$.

Also, many applications rely on high intensity THz sources that rely on further analysis of beam parameters such as spatial characterization of generated THz beam. To improve the knowledge about TPFP based terahertz sources with μJ-level energy I

have conducted measurements of parameters that are important in focusing and beam transportation – e.g. beam divergence angle and ellipticity of beam cross section – at various pump intensities.

Chapter 4

Generation efficiency dependence on pump pulse duration and temperature optimization

4.1 Introduction

In Chapter 2 I have covered all the necessary information for THz source and pulse characterization. In this Chapter I present scalability of the conversion efficiency for high-energy pulse generation.

Efficient pulse generation below 1 THz can be achieved in inorganic lithium niobate with tilted-pulse-front pumping [1]. Already demonstrated high-energy THz sources [2-5] predict that THz pulse energy up to 1 mJ can be attained. Theoretically it is predicted [16] that efficient laser source with 1 μm central wavelength and 600 fs transform-limited pulses would be optimal for pumping cryogenic-cooled LN based THz sources. My investigations aimed to experimentally find optimal pump parameters for efficient THz generation by verifying theoretical results. During the experiment OR was driven with variable duration, transform-limited pump pulses. I had the opportunity to perform experiments at Amplitude Systems (Pessac, France) with a

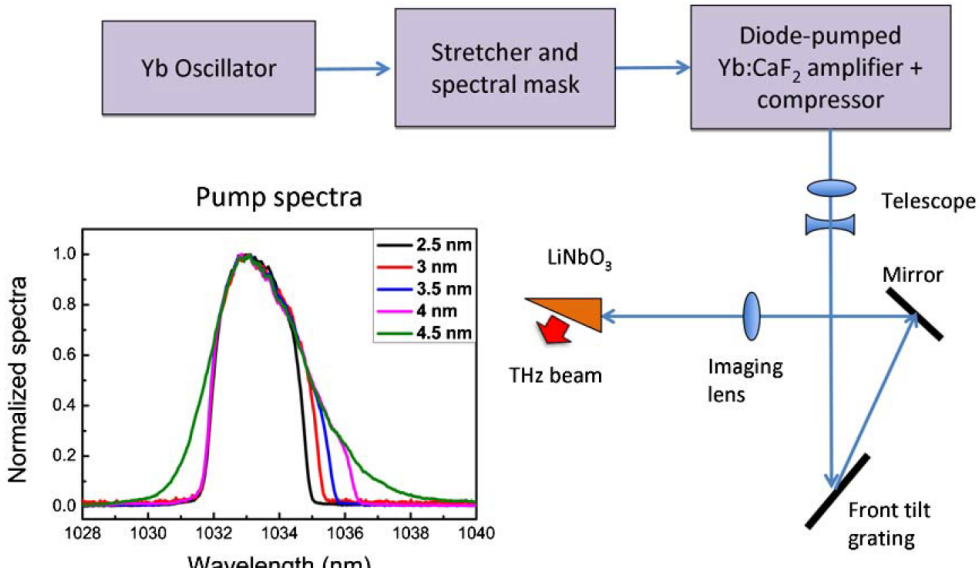

Figure 4.1: Experimental CPA laser setup [S1].

powerful, chirped-pulse amplification (CPA) Yb:CaF_2 laser system that consists of a compact ytterbium oscillator, a stretcher, a regenerative Yb:CaF_2 amplifier operated at RT, and a compressor. The broadband oscillator pulses were stretched to 500 ps before seeding into the regenerative amplifier. The amplifier gain medium was pumped by CW diode modules. After amplification, available uncompressed pulse energy was about 30 mJ at 10 Hz repetition rate. The CPA system was designed so that both narrowband and broadband pulses could seed the amplifier without damaging it. Figure 4.1 inset shows the different seeded, pre-shaped pulse spectral widths recorded after the compressor, resulting pulse lengths from 380 fs to 650 fs, near-Fourier-limited (FL) pulses up to 15 mJ.

The intense pump laser beam first was reduced by a 3:1 telescope and directed to a THz generation setup (Figure 4.2). For the generation of the THz pulses pulse-front tilting was realized by a 1400-lines / mm grating. Afterwards a $\lambda/2$ plate was placed in the path of the beam to rotate the diffracted and horizontally polarized pump to vertical polarization, so the polarization becomes parallel to the optic axis of the LN crystal. Subsequently, the grating surface was imaged into the LN crystal using a 25 cm focal length cylindrical lens. The OR was carried out in stoichiometric $LiNbO_3$, doped

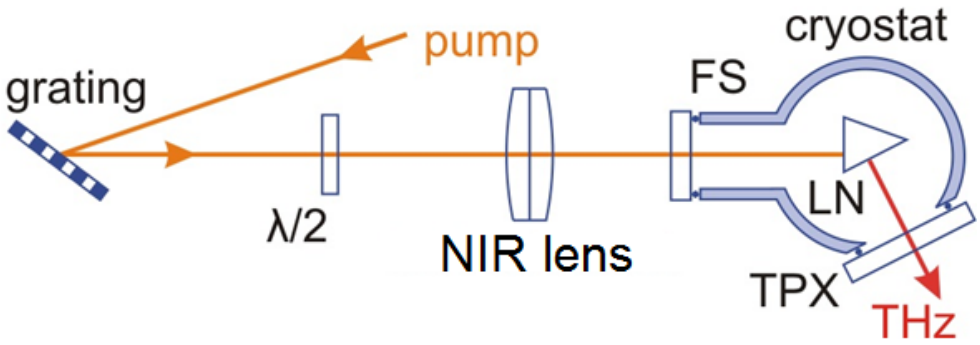

Figure 4.2: Tilted-pulse-front setup with single achromat lens imaging, and cryogenic cooled LN [S2].

with 0.6% MgO to increase optical damage resistance and reduce photorefractive effects [67-69]. The crystal had a 8 × 16 mm^2 (horizontal × vertical) useful size. Pump spot size of about 5 mm and energy up to 12 mJ was available to pump the LN crystal. The LN crystal was placed on a small aluminum table holder attached to the cold finger of a closed-cycle helium cryostat (Model 22 from Cryodyne). As velocity matching angle changes with temperature, pulse-front-tilt angle adjustment could be performed easily with the aid of the single lens imaging setup. Expected phase matching condition changes due to a 5% lower THz refractive index at CT [70] compared to RT was compensated by tilting the pump pulse front by 1.3°. As an input window for the pump beam I used a fused silica window with antireflection coating at the appropriate wavelength, and a TPX (polymethylpentene) window as an output for the THz beam. The chamber had an extended input tube for the pump beam to provide space for the focus plane of the NIR lens in vacuum to avoid nonlinear effects in air. The vacuum chamber of the cryostat was evacuated to about 10^{-6} mbar. Comparison measurements were carried out at RT (300 K) and at CT (23 K). LN and imaging lens position were readjusted to optimal generation at CT.

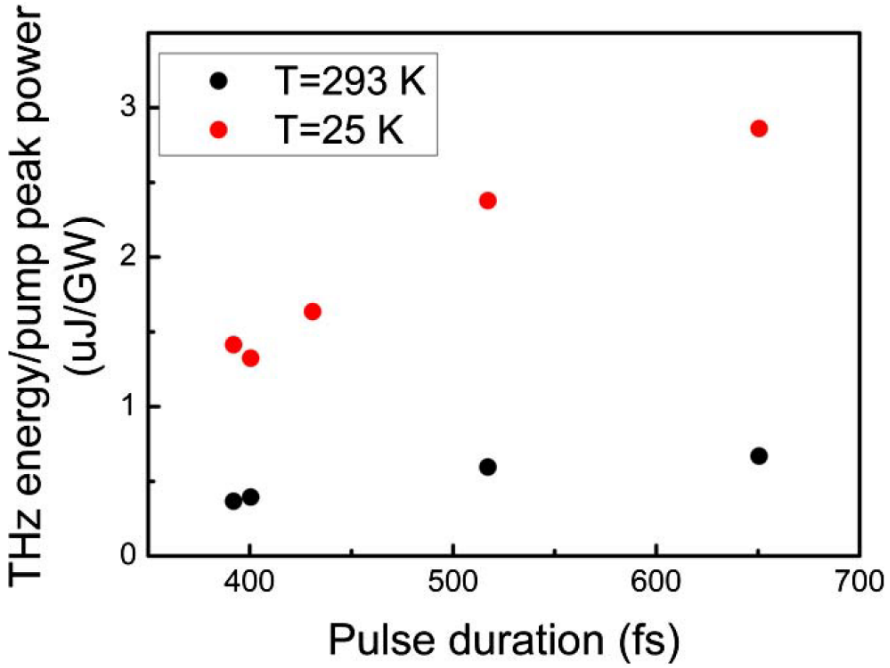

Figure 4.3: Measured THz pulse energy normalized to pump peak power vs laser pulse duration at RT (black) and CT (red) [S1].

4.2 Experimental results

The energy of the THz pulse was characterized by a calibrated Microtech $LiTaO_3$ pyroelectric detector with 3 kV / W responsivity. Figure 4.3 shows the THz energy, normalized to the pump peak power, as a function of the laser pulse duration for both RT and CT. As it was predicted from theory [16], investigations show a strong dependence of the conversion efficiency on the pulse duration. Maximum pump-to-THz conversion efficiency of 0.36% was reached with the 650-fs pulse, the longest pulse available from the current laser system. At this pulse duration conversion efficiency is twice as high as measured for the shortest pump pulse under the same conditions. I have conducted the same measurement series at RT and CT, and I observed similar behavior for both cases.

Although our main objective is to achieve higher conversion efficiency, it is worth investigating the induced effects also on the THz spectrum. Spectral measurements were performed with an in-air THz Michelson interferometer. I have recorded THz

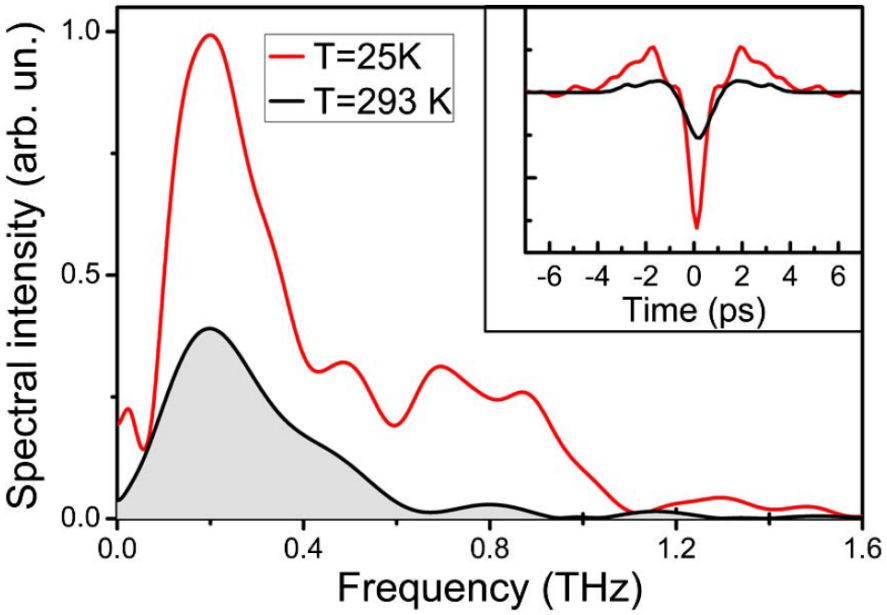

Figure 4.4: Measured THz spectral intensity profiles for 380 fs pump pulse at RT (black curve) and CT (red curve). Inset shows original recorded autocorrelation traces [S1].

spectra at RT (black curve in Figure 4.4) and CT (red curve in Figure 4.4), both generated with the shortest FL pump pulse and calculated by Fourier-transform (FT) of measured interferograms (inset of Figure 4.4). In Figure 4.4 spectral intensities are expressed in arbitrary units, yet the amplitudes can be directly compared and cryogenic cooling enhancements can be clearly observed. Due to the dramatic reduction of absorption in LN at higher frequencies the drop-off frequency shifts up to about 1 THz, so it is possible to cover the spectral region between 0.1 to 1 THz by cooling the LN source.

In our experiments conversion efficiencies measured are close to previously measured values at longer pulses [71]. Also, measured high pulse energy could result in a peak electric field of 2 MV / cm, by calculating the field with a central frequency of 0.4 THz, and assuming an imaging system with a numerical aperture of 1. As Figure 4.5 shows that shorter pump pulse duration gives rise to higher frequency components. It is worth noting that this along with cryogenic cooling helps to cover the full spectral range between 0.1 and 1 THz.

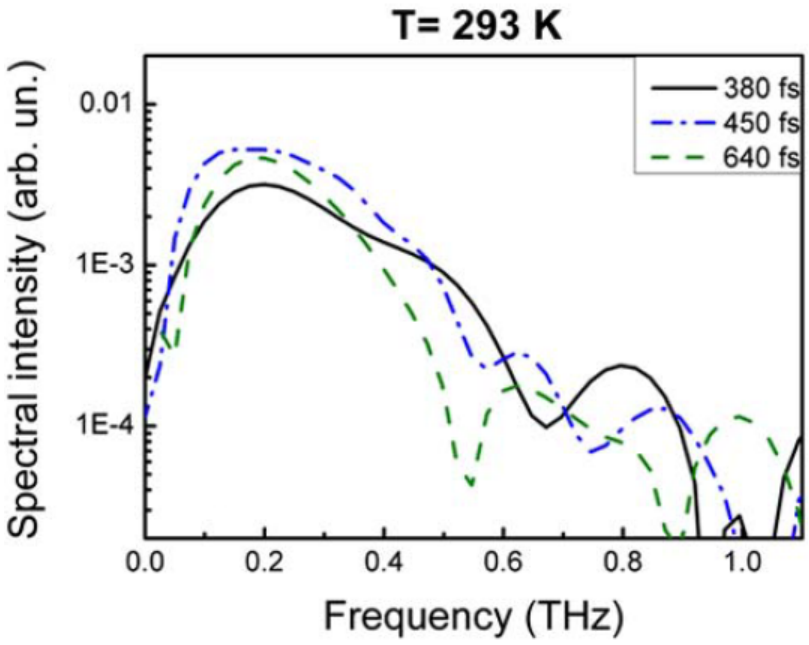

Figure 4.5: Recorded spectral intensities for different pump pulse durations [S1].

4.3 Discussion

I experimentally determined the optimal pump pulse duration to generate intense THz pulsesin LN, illuminated by a compact mJ level Yb:CaF_2 laser. I measured OR conversion efficiency and generated THz spectra for various LN source temperatures and pump pulse durations. I showed that the spectral range of 0.1 to 1 THz can be covered by using CT and the shortest accessible pump pulse duration. Nevertheless, longer pulses were advantageous to reach higher conversion efficiency (0.36%) and pulse energy (45 μJ). For all pump pulse durations cooling of LN yields higher conversion efficiency and higher frequency components due to reduced absorption.

Chapter 5

Cryogenic cooling impact on generation efficiency

5.1 Introduction

An evolving set of motivating new applications will require THz pulses with particularly high energy in the multi-mJ range. Acceleration, longitudinal compression, and undulation of relativistic electron bunches [10,21], leading to single- or few-cycle femtosecond or attosecond pulse generation, or the post-acceleration of laser-generated proton and ion beams with potential applications for hadron therapy [36] could benefit from the developing high energy THz sources in the future. A significant advantage of THz sources is the generated lower-frequency range (0.1 to 3 THz) over visible laser sources, infrared laser pulses [2,71] or other type of THz sources [72]. Longer wavelength is ideally matching typical transversal sizes of particle beams, which are on the order of 100 μm.

Present-day sources having extremely high field strengths up to 100 MV/cm are available only in the higher frequency range (above 10 THz) of the THz spectrum [1]. The energy and peak electric field of accessible intense table-top sources in the low-frequency THz part is one or two orders of magnitude below the required level [3-5,15-17].

In the previous chapter I have covered a key part: optimization of the Fourier-limited (FL) pump pulse duration for high-energy and efficient THz sources. The proposals and predictions of theoretical studies [54,73,74] show that cooling LN to cryogenic temperature (CT) in order to reduce its THz absorption is the next large step towards achieving multi-mJ systems in the lower frequency range.

5.2 Experiment for moderate THz energies

The setup described in the previous chapter (Figure 4.2) made cooling the LN source to CT realizable. Figure 4.3 shows measured THz pulse energy, normalized to the pump peak power, as a function of the laser pulse duration for both RT and CT. Experimental comparison show that maximum conversion efficiency achieved at RT is 0.12% and at CT 0.36%, where the largest THz pulse energy reached 45 μJ.

5.3 Experimental description for higher THz energies

In a set of experiments I compared high-energy THz pulse generation at RT and CT (Section 4.1, Figure 4.2), however pumped by a high-energy sub-picosecond Yb:YAG chirped-pulse amplification system at 10 Hz, 1030 nm central wavelength, 3.4 nm FWHM spectral bandwidth and pulses compressed to about 785 fs duration [75] to obtain the highest possible THz pulse energies. The imaging lens was replaced by a 20 cm focal length, 50 mm diameter near-infrared achromat lens. Pump spot size was rather large on the front surface, 10.4 mm in the horizontal direction and 15.3 mm in the vertical direction. This was slightly larger than the effective horizontal size of LN (8.1 mm).

The generated THz beam is highly divergent so the divergent beam was imaged by a 6-inch effective focal length (EFL), 2-inch diameter, 90° deviation off-axis parabolic

(OAP) mirror and a 2-inch EFL, 2-inch diameter, 90° OAP mirror. That gives a magnification ratio of 1/3. Knife-edge technique was used to determine the focal spot size in the focal plane of the second OAP mirror. Temporal waveform profile was also recorded, by EOS of the THz pulse at the knife-edge measurements position. The knife was replaced by a 0.1 mm thick (110)-cut ZnTe active layer, attached to a 1 mm thick inactive ZnTe bulk. A pair of wiregrid polarizers (WGP) were used to reduce the THz beam intensity to avoid the over-rotation of the induced birefringence in ZnTe [76]. The 0th-order reflection from the grating was taken as probe for EOS. Reflection-type EOS geometry was used, where THz beam and pump beam arrive at the detector crystal from opposite directions. The probe then internally reflects from the outside surface of the active layer of the EO crystal, so after reflection it could co-propagate with the THz beam and the probe beam can detect the THz signal. The EOS signal was recorded by balanced detection technique, consisting of a $\lambda/4$ plate, a Wollaston prism, and two identical photodiodes. A lock-in amplifier with 10 Hz reference signal and the average of 3 pulses were used to improve the signal-to-noise ratio.

Calculations of Fülöp et al. in [16] predict that THz generation efficiency (η) can be improved by a factor of 3 to 6 while cooling the LN source. The enhancement factor depends on the pump pulse duration and LN crystal temperature. Estimated enhancement factor is η_{CT}/η_{RT} ≈3 to 4 for 785 fs pump pulse duration. Previous experimental studies [71,77] have already investigated this effect. However, our goal was to show this at much higher energies, in the 100 μJ-level THz pulse energies. Cooling LN from RT to CT results in a refractive index change and thus in a small but substantial deviation of the pulse–front–tilt angle required for pump velocity – THz velocity matching. Consequently, an angle adjustment is needed. This can easily be done in a single lens TPFP setup by shifting the lens. Available maximum pump energy was 30 mJ, with a maximum intensity of 23.6 GW cm^{-2}. Figure 5.1 shows measured THz energies at RT and CT as a function of pump energy and intensity at the LN crystal. Throughout the measured range a continuous increase of THz energy can be observed. Maximum THz

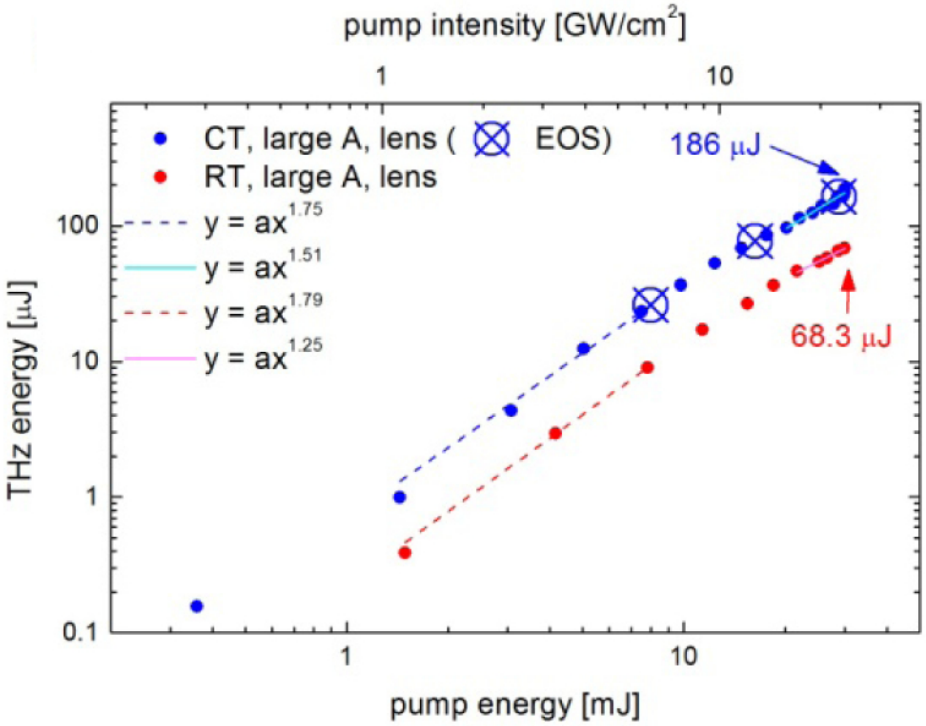

Figure 5.1: Measured THz energy dependence on pump energy and intensity at RT (red) and CT (blue). At the marked crosses EO measurement was carried out [S2].

energy is approximately 2.7-times higher at CT (186 μJ) than at RT (68 μJ), which is in good agreement with mentioned calculations [16]. The measured increase is due to the reduced absorption of LN at CT [16]. However, a decrease can be observed in the fitted power exponent (Figure 5.1) from 1.8 below 10 mJ to 1.5 above 20 mJ at CT and from 1.8 to 1.3 at RT. Figure 16 shows the matching pump-to-THz energy conversion efficiencies as functions of the useful pump energy and intensity. It can be read from the figure that up to 15 mJ (12 GW cm^{-2} intensity) a conversion efficiency growth can be achieved. Above this level efficiencies increase at a reduced rate. Maximum calculated efficiencies were 0.62% (CT) and 0.23% (RT). Ratio of the CT and RT efficiencies η_{CT}/η_{RT} (empty symbols in Figure 5.3) varies around 2.7 below 15 mJ pump energy, which is somewhat lower than predicted by calculations. A noticeable drop to 2.5 can be seen in the range of 15 to 20 mJ pump energies (12 GW cm^{-2} and 16 GW cm^{-2} intensities). At higher pump energies the enhancement factor increases

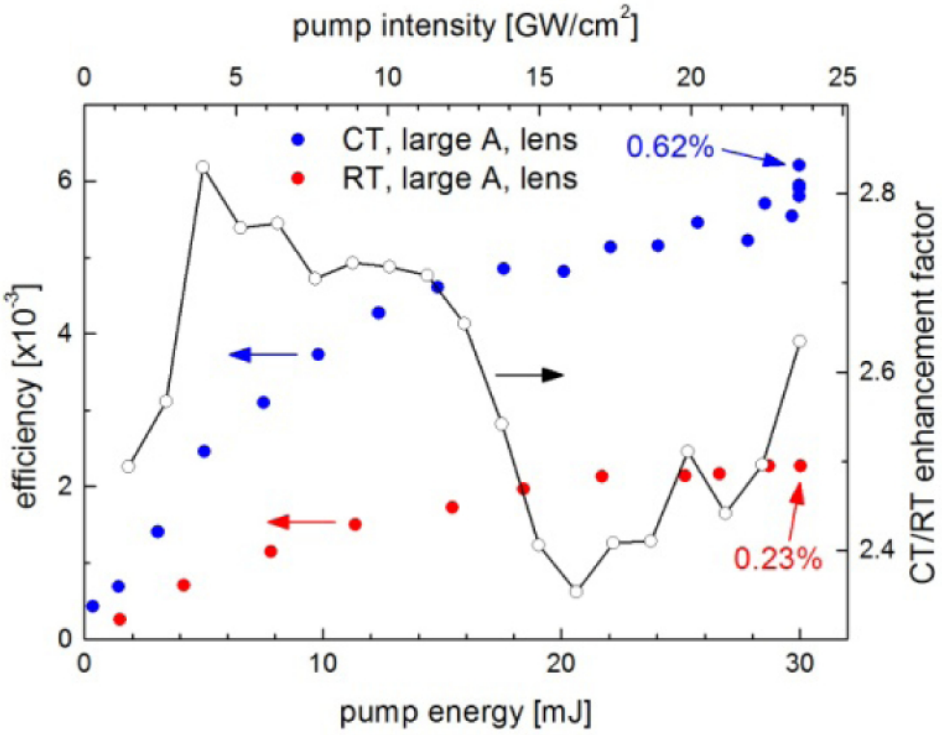

Figure 5.2: Conversion efficiency for RT (red) and CT (blue), and the ratio of CT and RT efficiencies (black) vs. pump energy and intensity [S2].

gradually from about 2.4 to 2.6.

5.4 Experimentally demonstrated pulses that are applicable for charged pulse manipulation

High-energy THz pulse applications require precise characterization of the pulses. Relevant parameters are temporal waveform and corresponding spectrum, beam focusability, and pulse energy. These parameters altogether define maximum reachable focused peak electric field. Besides energy measurements (shown in Section 5.3) we also carried out electro-optic sampling and focal spot measurements to determine the necessary parameters.

The characterized pulses were generated with the setup described in Section 5.3 using a single achromatic lens for imaging, and a large pumped area at cryogenic tempera-

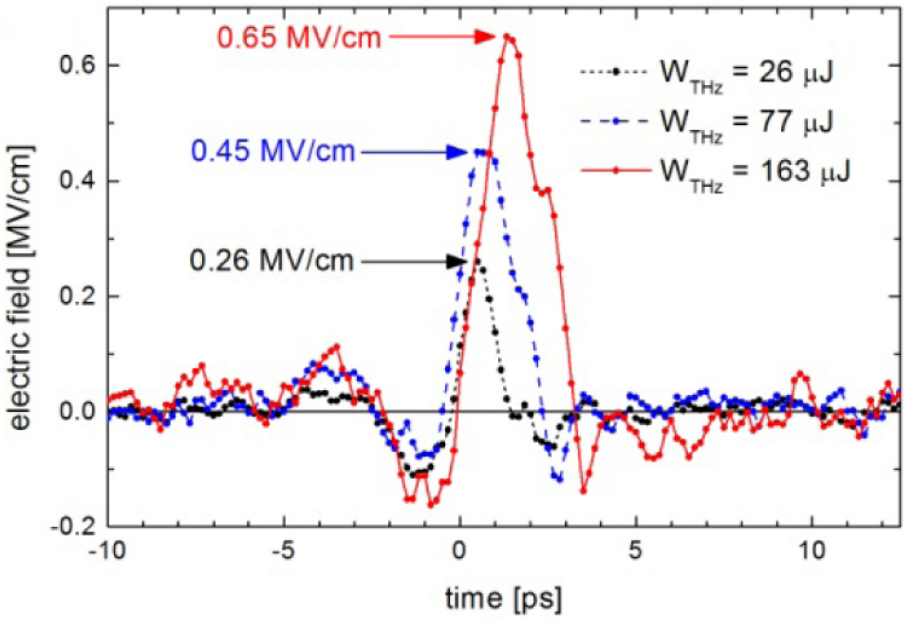

Figure 5.3: Measured time dependent electric field at high THz energies [S2].

ture. Figure 5.3 shows examples of in-focus waveforms measured by an electro-optic sampling setup, for three different THz pulse energies: W_{THz} = 26 μJ, 77 μJ, and 163 μJ, corresponding to 7.8 mJ, 16 mJ, and 29 mJ pump energies, respectively. A strong asymmetric behavior of the waveform is observed, which contains less than a full oscillation cycle, with only one leading half-cycle. The pulses show a positive chirp. Noticeable strong noise primarily comes from the low repetition rate of the laser.

With increasing THz pulse energy, one can identify a clear shift of the main frequency toward lower values. Figure 5.4 shows obtained spectral amplitudes of the THz pulses, calculated by Fourier transformation from pulse waveforms shown in Figure 5.3. The spectra cover the 0.05-1 THz range in all cases. An intense, low-frequency part up to around 0.4 THz can be observed, followed by an order of magnitude smaller spectral amplitude part extending to about 1 THz. Simulations based on the model described in [15] show slightly broader spectra ranging beyond 1 THz, though with a more uniform distribution pattern, without any decreased parts at 0.4 THz (Figure 5.4

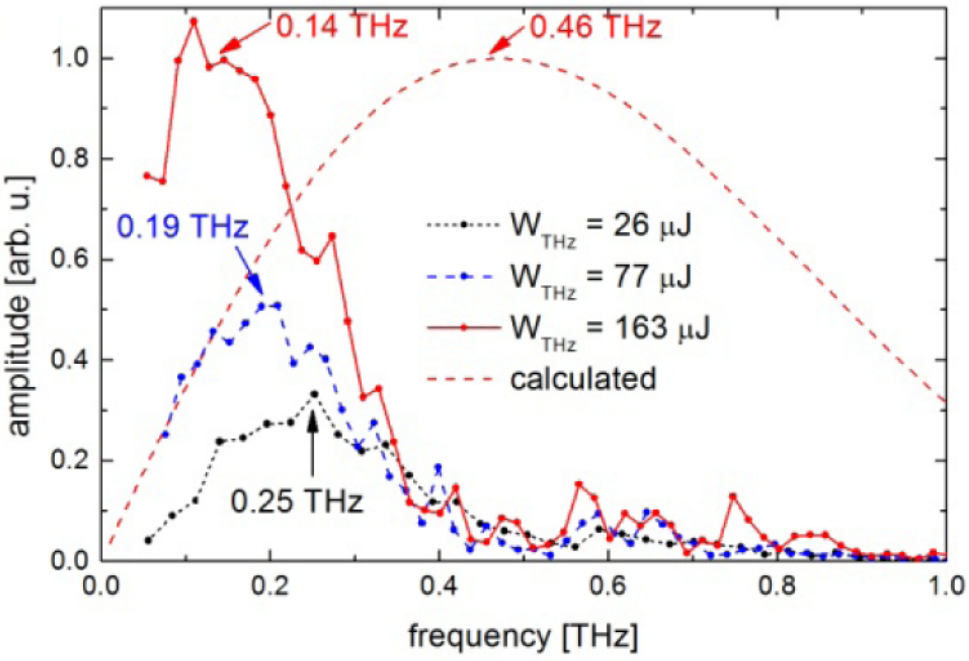

Figure 5.4: Spectral amplitudes obtained from the waveforms of Figure 5.3 by Fourier transformation, in comparison with the calculated spectrum [S2].

dashed curve without symbols).

I have also investigated focal spot size by the knife-edge method for the highest (29 mJ) pump energy. Measured THz energies as function of the knife-edge position are shown in Figure 5.5 for horizontal and vertical scan directions. Gaussian beam fittings overlap well with the recorded data points. Fitted values for $1/e^2$ horizontal and vertical radii are w_H=2.4 mm and w_V=2.7 mm, respectively.

Peak electric field strengths are 0.26 MV/cm, 0.45 MV/cm, and 0.65 MV/cm calculated from the measured waveform Figure 5.3), focal spot size, and for pulse energies of 26 μJ, 77 μJ, 163 μJ, respectively. Albeit these electric field values seem weak compared to other experiments [14,21,78], the significantly lower main THz frequencies should be taken into account. To our knowledge, pulses generated in the low-frequency range in our experiment have the highest measured electric fields reported to date.

Additionally, we noticed a consistent decrease in the main frequency of the spectral peak while increasing the pump pulse and THz energy. Main frequency is about 0.25

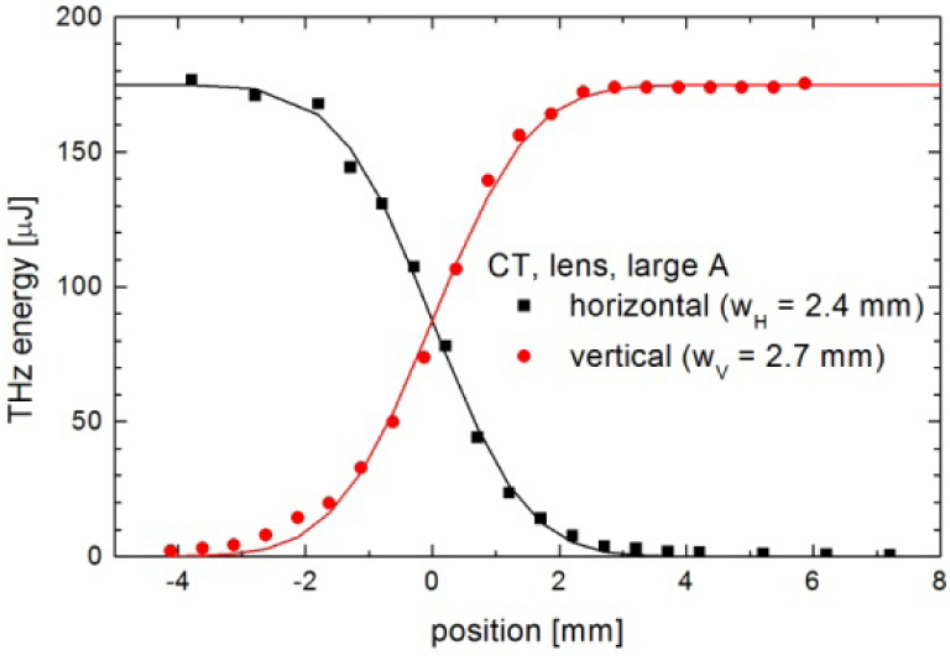

Figure 5.5: Measured focal spot size by knife-edge scan. Fitted curves correspond to assumed elliptical Gaussian profiles [S2].

THz for 26 μJ THz energy at a moderate pump pulse energy, which reduces to its half, 0.14 THz for 163 μJ. However, simulations in [15] show no energy dependence of the THz spectra. It is also worth noting that observed width of spectra show no energy dependence. Gaussian fit to the prominent low-frequency part gives spectral FWHM values in the 0.27 THz to 0.24 THz range. Possible further investigation and explanation of the revealed features are beyond the scope of this thesis.

5.5 Discussion

Precise characterization of high energy pulses and measurements of waveform are crucial while scaling up THz sources. The data I gathered can be important in designing highest-energy THz sources and application, regarding expected spectral frequency range and necessary pump pulse energy.

The achieved high energy THz pulses in the low frequency range could be beneficial for charged-particle manipulation [12,79]. Also, peak electric field strength is suitable

for acceleration experiments. Current results predict that THz energy can be increased above 1 mJ with only 100 mJ pump pulse energy, cryogenic cooling and optimal pulse duration.

Chapter 6

Lithium niobate based source illuminated by increased pump intensity

6.1 Introduction

Optimizations predict that THz sources can be scaled near to mJ level. I have conducted measurements to increase THz pulse energy to the highest possible value. A tilted-pulse-front pumping setup (Figure 6.1) was built with two-lens imaging. Ray-tracing shows optimal imaging conditions [15] [80] for smaller curvature of the tilted-pulse-front compared to a single lens imaging. This property is advantageous for high conversion efficiency, particularly at large pumped areas. The two-lens imaging was built by a 25-cm focal length, 50-mm diameter and a 15-cm focal length, 25-mm diameter lenses in confocal arrangement. Pumping the built setup was done by the same laser as described in Section 5.3 (1030 nm central wavelength and 785 fs pulse duration). To avoid nonlinear effects in air a vacuum tube was placed at the focal plane of the first lens. Furthermore, before the conventional TPFP a 2.5:1 demagnifying telescope was built to reduce pump area and to attain high pump intensities at the source crystal.

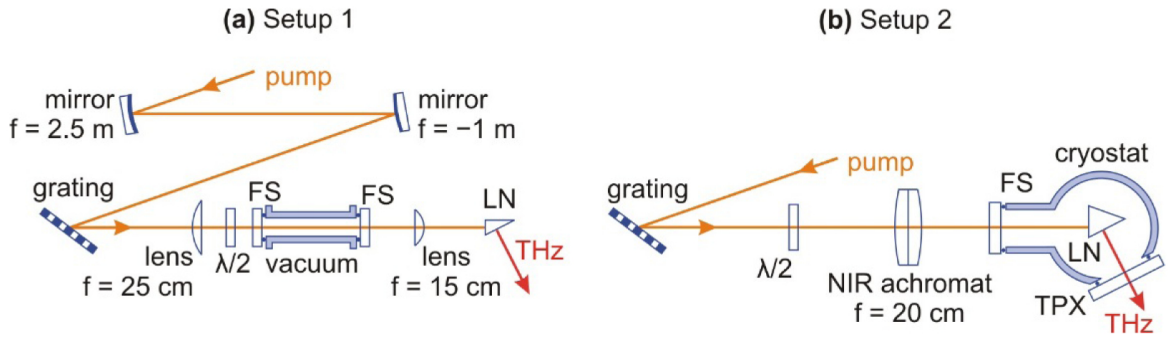

Figure 6.1: TPFP setup with beam-narrowing and imaging telescope for highest THz energies [S2].

The obtained pumped area on the crystal surface was rather small, with a diameter of 5.6 mm × 7.0 mm (horizontal × vertical) at full width at half-maximum (FWHM).

THz beam was coupled into a calibrated Microtech Instruments pyroelectric detector to measure pulse energy. To avoid saturation of the detector a 0.5 mm silicon wafer (70 % measured THz transmission) and black cardboard (80 % measured THz transmission) were placed in front of the detector to block fundamental pump and second harmonic optical radiation. To check for possible detector saturation, additional attenuator cardboard plates were used. For THz beam size and temporal profile measurements the same technique was used as described in Chapter 5.

6.2 Experimental results

Figure 6.2 shows measured THz energy at RT as a function of the pump energy. Measured maximum pump energy entering LN crystal was 58 mJ, which corresponds to 237 GW cm^{-2} intensity. I have observed a monotonic increase of the THz energy with increasing pump energy. Previous observations using much longer (1.3 ps) pump pulses [16] differ significantly, where THz energy started to saturate, then decrease above 45 mJ pump energy. Closer investigation of the results was done by fitting power functions to measured data for different pump energies. Results show a slight decrease in the power exponent – 1.5 below 10 mJ and 1.4 between 10 mJ and 30 mJ – then

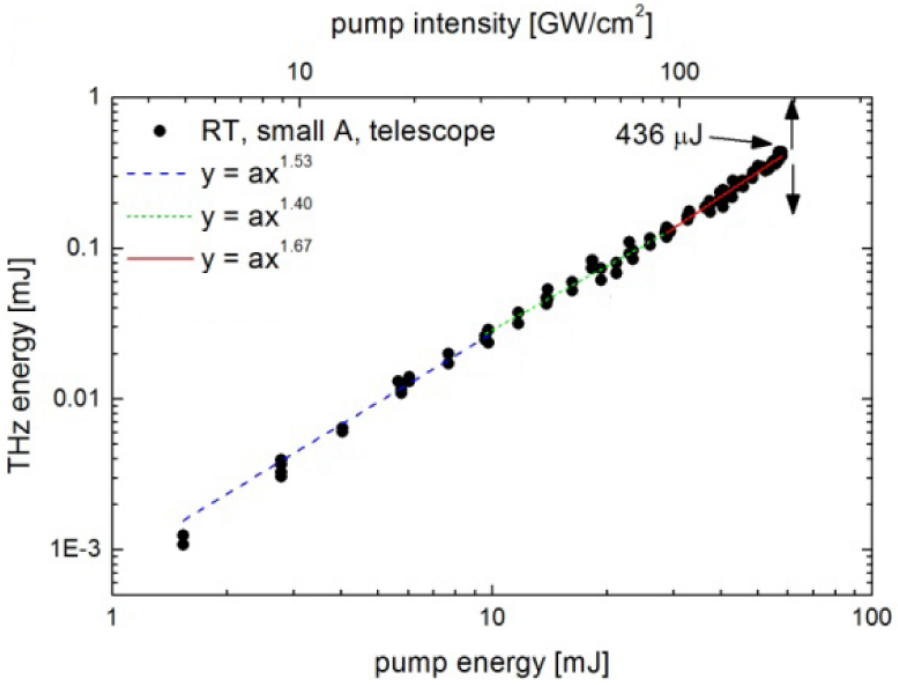

Figure 6.2: Measured THz energy dependence on pump energy and intensity [S2].

an unexpected rise to 1.7 above 30 mJ. This can be explained by the saturation of free-carrier absorption, similar to the case with ZnTe [81].

Maximum THz energy achieved with the current setup was as high as 436 μJ, at 58 mJ pump energy. This corresponds to a pump-to-THz energy conversion efficiency up to 0.77 %. Figure 6.3 shows calculated efficiencies as a function of the pump fluence. At the saturation point of the previous experiment (about 150 mJ cm^{-2} fluence) calculated efficiency was two times higher with shorter pump pulse, 785 fs, than with 1.3 ps pulses. This agrees well with calculations in [2], which predict 2.3-times higher values for pump pulses closer to optimum pumping.

6.3 Discussion

Experiments were conducted by illuminating a room temperature lithium niobate crystal in a pulse front tilting setup with large pump intensity and a rather small spot size

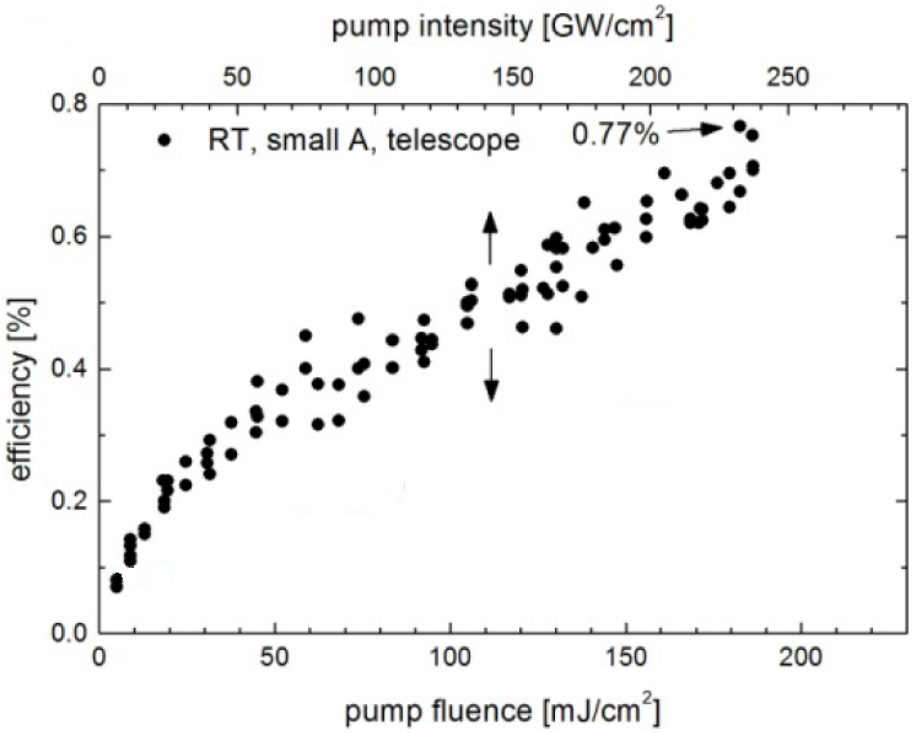

Figure 6.3: Calculated efficiencies vs. pump fluence and intensity [S2].

of 5.6 mm × 7.0 mm (horizontal × vertical) in combination with optimal imaging (25-cm focal-length and 15-cm focal-length in confocal arrangement), and nearly optimal pump pulse (785 fs). I have demonstrated highest pulse energy up to 0.4 mJ in the lower THz frequency range. I reached a generation efficiency of 0.77% which is the highest demonstrated for large THz pulse energies.

Chapter 7

Generation efficiency limitations

7.1 Introduction

As the previous chapters were dealing with my primary attention – to optimize THz sources and generate the highest possible THz pulse energies – I also should concentrate on the effects due to increased energy on efficiency. Pump angular dispersion limitations were already investigated for TPFP THz sources [15,16]. Conversion efficiency saturation [2,82] and pump self-phase modulation [82] were also reported. Pump pulse – THz field nonlinear interaction shows also a limitation effect on the THz generation interaction length [83].

Many applications rely on high intensity THz sources [10,11,13]. Nevertheless, these experiments assume ideal beam parameters, which is usually not the case for lab experiments. Further analysis of beam parameters such as spatial characterization of generated THz beam is unavoidable, though some methods have already been developed [84-86]. Recent studies examined the spatial emission characteristics of air plasma THz sources [86,87]. However, less detailed experiments were completed for TPFP in LN sources [88]. Theoretical calculations show that imaging system distortions can lead to highly distorted THz beam profiles [15], although nonlinear effects were ne-

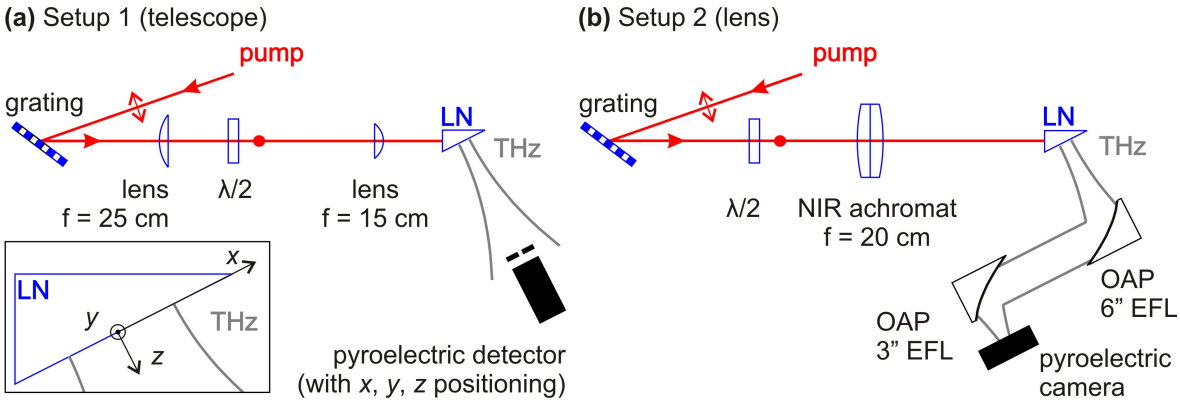

Figure 7.1: Experimental setup: (a) Setup 1 with the imaging telescope; (b) Setup 2 with the NIR achromatic lens. LN: $LiNbO_3$ prism, OAP: off-axis parabolic mirror, EFL: effective focal length. The inset in (a) shows the definition of the coordinate system [S3].

glected. Also, high-field, and nonlinear THz spectroscopic applications could benefit from thorough consideration of THz beam distortions induced by focusing and beam transport optics.

To improve the knowledge about TPFP based sources I have investigated the properties of THz beams generated in LN crystals with μJ-level energy. I have conducted measurements of parameters that are important in focusing and beam transportation – e.g. beam divergence angle and ellipticity of beam cross section – at various pump intensities.

7.2 Experimental setup

Throughout my experiments I used an Yb:CaF_2 regenerative amplifier (200 fs pulse length, 1 kHz repetition rate, 1030 nm central wavelength) as pump laser. Pulses were generated by illuminating a stoichiometric LN (0.6% MgO doping) prism at room temperature with a TPFP setup. I have conducted the measurements with two setups, using the corresponding optimal imaging conditions [2,8].

In Setup 1 (Figure 7.1(a)) a 1400 lines / mm grating was used to tilt the pump

pulse front. A retardation plate was used after the grating to rotate pump polarization direction parallel to the optical axis of the LN source crystal. Imaging was realized by a telescope consisting of a 250 mm and a 150 mm focal length lens in confocal arrangement. Available maximum pump energy at the source crystal was 5.8 mJ, where the crystal was illuminated on a 3.8 mm $\times$ 5.6 mm ($1/e^2$) area. Calculated maximum fluence was nearly 35 mJ cm^{-2}, the corresponding intensity was 177 GW cm^{-2}.

Telescope imaging was later replaced by a single, near-infrared achromatic lens imaging with 200 mm focal length. For this configuration (Setup 2, Figure 7.1(b)), available maximum pump energy was 6.3 mJ and the illuminated area on the source crystal was about 4.0 mm $\times$ 4.9 mm. Calculations give a pump fluence of 41 mJ cm^{-2} and 205 GW cm^{-2} intensity.

After optimization of the room temperature LN source I have measured the generated THz energy by a calibrated pyroelectric detector (Microtech Instruments). The obtained 9 μJ energy corresponds to a maximum of 0.15% generation efficiency. Temporal waveform was also recorded to get information about the frequency spectrum of the sources. THz pulse waveforms were measured by electro-optic sampling using a (110)-oriented 0.1 mm thick active layer on a 2 mm thick inactive ZnTe substrate.

Cross sections of the THz beam profile were recorded at different distances from the source crystal by using a horizontal (x-axis), vertical (y-axis) and a third translation stage (z-axis). Point-to-point measurements were conducted by a sensitive, large-area pyroelectric detector (Gentec QS9-THz-BL, Figure 2.5(right)). Pump radiation and second harmonic radiation were blocked by a black cardboard and a 0.5 mm silicon wafer. To avoid spatial averaging a variable-aperture iris diaphragm was placed in front of the detector. The iris aperture size was chosen so as to fit between 5% and 20% of the $1/e^2$ THz beam diameter at each z-position. Near-field THz beam profiles

were recorded in Setup 2 using a two-dimensional pyroelectric profiler (Ophir Pyrocam III). While the THz beam was larger than the camera's available 1/2" sensor size, the LN crystal's output surface was imaged with a 2:1 demagnification on the camera by two off-axis parabolic (OAP) mirrors Figure (7.1(b)). Demagnification was made by 6" and 3" effective focal length, 2"-diameter OAP mirrors, respectively.

7.3 Far-field measurement

The presented experimental setups have helped to conduct transversal beam profile scans for both horizontal and vertical sections up to z=430 mm distance from the LN crystal output surface. I carried out measurements at a few pump levels for all profiles with both Setup 1 and Setup 2. Figure 7.2 (a) and (b) shows example cross sections of the recorded THz beam for z=310 mm . I have noticed that THz beam width has increased with increasing pump intensities. The observed increase was stronger for the telescope imaging version (Setup 1). Based on the recorded data I carried out calculations of THz beam parameters, like divergence in the horizontal and vertical plane. Gaussian beam propagation formula was fitted on the recorded profiles, so I could determine horizontal (H) and vertical (V) beam radii w_H (z) and w_V (z), respectively. Also, divergence angles $\theta_{(0,H)}$ and $\theta_{(0,V)}$ were calculated as half opening angles of the beam [21]. During beam propagation fitting supposing a central frequency of 0.33 THz was used, which corresponds to the maxima of the FT of the measured THz temporal profile (Figure 7.3). Position and beam waist size were used as optimization parameters. Obtained beam radii are shown in Figure 7.2(c) and Figure 7.2(e) for the telescopic imaging setup, and Figure 7.2(d) and Figure 7.2(f) for the single lens imaging setup, respectively.

Observations show that beam divergence in the horizontal plane increased with increasing pump fluence (Figure 7.2(d)), although in the vertical plane it remained

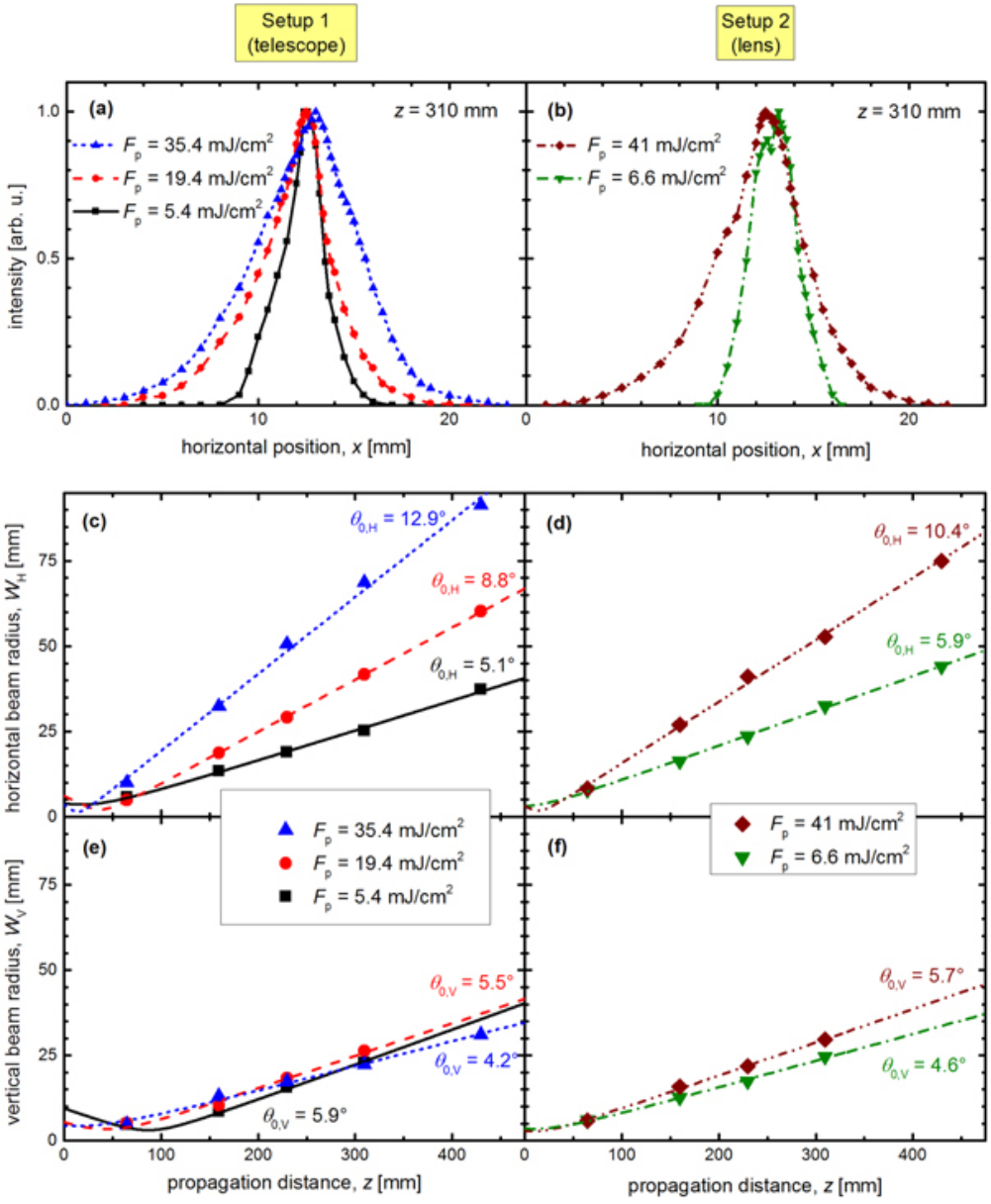

Figure 7.2: Examples of measured THz beam profiles for different pump intensities at z=310 mm for Setup 1 (a) and Setup 2 (b). Observed variation of horizontal (c) and vertical (e) THz beam radii as a function of the propagation distance z for Setup 1 (telescope). (d), (f) show the corresponding radii for Setup 2 (lens) [S3].

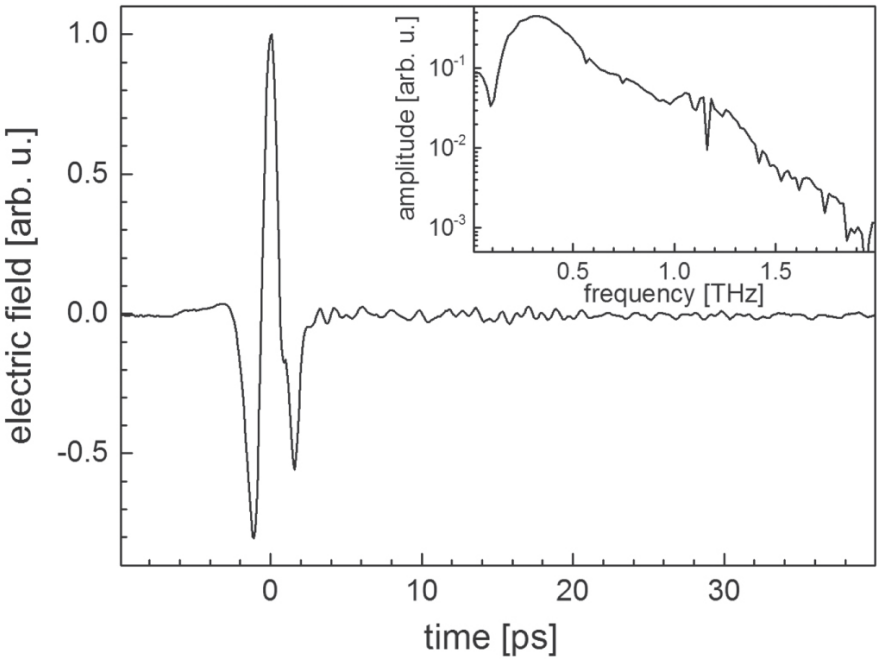

Figure 7.3: THz waveform measured by electro-optic sampling and the corresponding THz spectrum in the inset calculated by Fourier transformation [S3].

unaffected (Figure 7.2(f)). As for the telescopic imaging setup at the lowest measured pump fluence (5.4 mJ cm^{-2}) a horizontal divergence angle of 5.1° was calculated which value increased to 12.9° at the measured highest pump fluence (35.4 mJ cm^{-2}, Figure 7.2(c)). However, in the vertical plane the divergence angle – 4°- 6° – did not change significantly for all the measured pump fluence levels (Figure 7.2(e)). Comparable results were given for the single lens imaging setup. The variation of the horizontal divergence angle was somewhat smaller, for the lowest measured pump level: (6.6 mJ cm^{-2} pump fluence) 5.9° was calculated, and has increased at the highest measured pump level (41 mJ cm^{-2} pump fluence) to about 10.4° (Figure 7.2(d)). A possible explanation of the observed behavior could be the difference in imaging distortions of the setups that can induce differences in the pump pulse fronts and therefore changes in the THz phase front curvature [15].

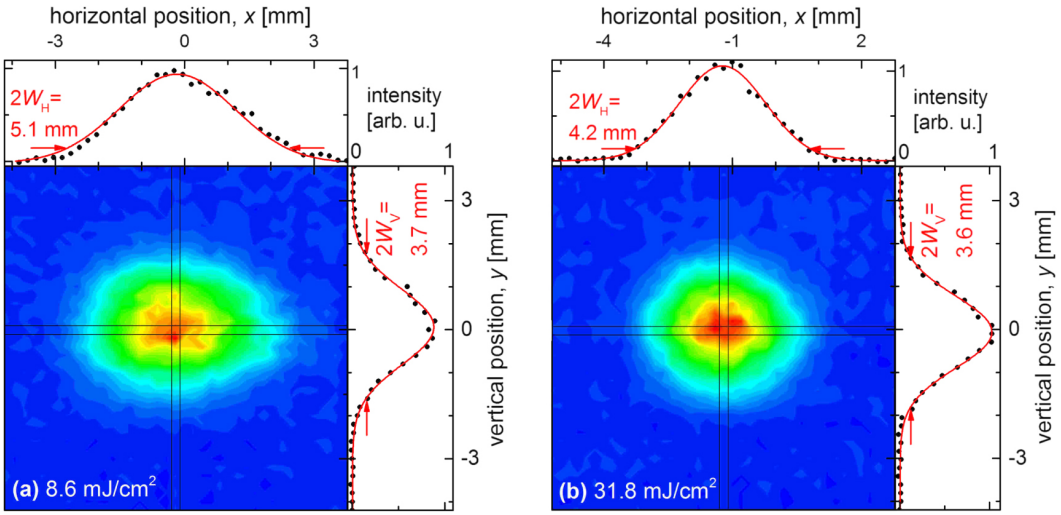

Figure 7.4: Measured two-dimensional near-field THz intensity beam profiles at (a) 8.6 mJ cm^{-2} and (b) 31.8 mJ cm^{-2} pump fluence. The insets show the respective central one-dimensional profiles [S3].

7.4 Near-field imaging

Applying a demagnification off-axis parabolic mirror imaging made near-field measurements available. I have built an OAP mirror pair with 2:1 focus ratio to observe near-field intensity profiles of LN crystal using a pyroelectric camera (Spiricon Pyrocam III, Figure 6) in Setup 2 (Figure 7.1(b)). I recorded beam profiles at various pump fluence levels. Figure 7.4 shows THz beam profiles, rescaled to compensate the demagnification. Recorded THz beam profiles were elliptical with $1/e^2$ half-widths of w_H=2.5 mm and w_V=1.8 mm, corresponding to an axis ratio of w_H/w_V =1.38, for Figure 7.4(a) at lowest measured pump fluence (8.6 mJ cm^{-2}). I have noticed that for the highest measured pump fluence (31.8 mJ cm^{-2}) horizontal half-width has reduced to w_H=2.1 mm , while there was no significant change for the vertical axis where measured half-width was w_V=1.8 mm (Figure 7.4(b)). These values correspond to an axis size ratio of w_H/w_V = 1.19.

Measurements show a monotonic decrease in the horizontal spot size, changing from 2.5 mm to 2.1 mm, while pump fluence varies from 5.3 mJ cm^{-2} to 31.8 mJ cm^{-2}, respectively. In the vertical size no significant change can be seen. Measured THz spot

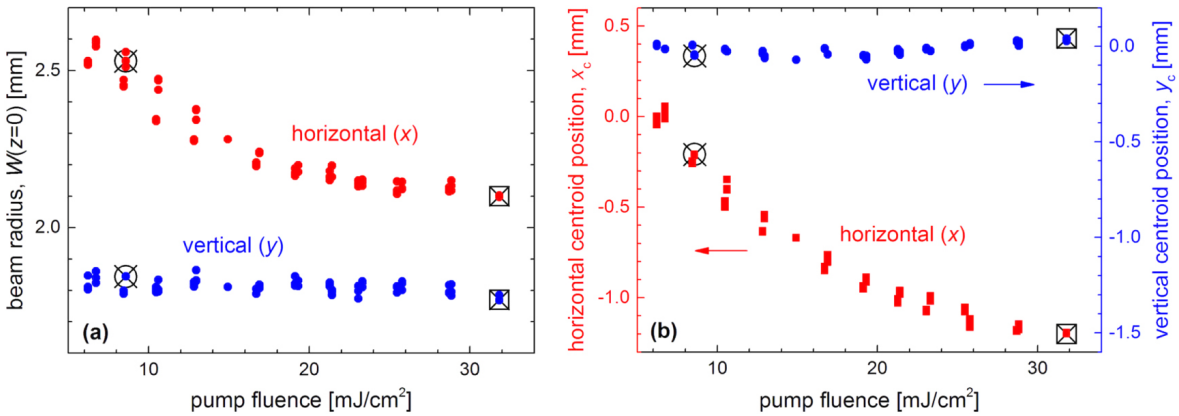

Figure 7.5: Measured horizontal and vertical near-field THz beam radii (a) and positions of near-field THz beam centroid (b) as a function of the pump fluence. The data points with the crossed circle and square symbols correspond to the beam profiles in Figure 7.4(a), (b), respectively [S3].

radii as a function of pump fluence are shown in Figure 7.5(a). This observation is in a good agreement with far-field – beam divergence – measurement results. Figure 7.5(b) shows center positions as a function of fluence for both horizontal and vertical axes. A shift can be seen towards the crystal apex direction ($(-x)$ direction in Figure 7.1 inset). However, there is no change in the vertical center position.

THz beam variation in the horizontal axis can be seen for both conducted measurements with varying pump fluence, while no change could be seen in the vertical axis. The observed phenomena can be explained with the change of effective interaction length of THz generation. In case of large diameter pump beams, as in our setup, interaction length variation is determined by the pump pulse duration along the propagation distance inside the LN source crystal due to material and angular dispersion, and THz absorption in LN [15,16]. At large pump intensities generated THz field can be strong enough to alter the pump pulse spectrum [83,89,90]. Pump pulse can be also influenced by self-phase modulation [82].

7.5 Discussion

Experiments were conducted for TPFP LN THz sources pumped by 200 fs laser pulses to determine near-field and far-field THz beam profiles and THz divergence angles. I have observed that the increase in the pump fluence leads to the decrease in horizontal near-field beam diameter which is in a good agreement with increasing divergence angle. However, there was no change found in the vertical direction. The noticed nonlinear behavior of THz beam properties was explained by the interplay between intensity-dependent interaction length and non-collinear phase-matching geometry of the TPFP scheme.

Results show that in addition to efficiency optimization, care should be taken on THz beam properties, too. The noticed change of the THz beam properties on the pump fluence is important for designing high field THz sources and their applications involving any kind of beam transport and focusing. For applications where aperture is limited, nonlinear variation of THz beam divergence can also affect spectral transmissions. My results are significant for the developing research fields of THz nonlinear spectroscopy and high-field THz science.

Chapter 8

Thesis statements

Thesis statment 1 With the aim to increase pump-to-THz generation efficiency I have investigated a THz source based on optical rectification of femtosecond laser pulses with tilted-pulse-front pumping in a lithium niobate crystal illuminated with variable-duration transform-limited pulses. I have shown that longer pump pulses are favourable for reaching higher conversion efficiency, in accordance with the general trend predicted by theoretical calculations [S1]. Moreover, I have shown that a broader THz spectrum can be achieved by using shorter pulses.

Thesis statment 2 THz generation efficiency investigations were carried out by building diverse cryogenic-cooled THz sources based on tilted-pulse-front pumping in a lithium niobate crystal. I have shown up to 45μJ THz pulse energy that the conversion efficiency can be increased by a factor of 4 using cryogenic cooling of the source crystal. Above 50μJ about up to 180μJ an enhancement factor of 2.4 was demonstrated. [S1, S2]

Thesis statment 3 By illuminating a room temperature lithium niobate crystal in a pulse front tilting setup with large pump energy and a large pump intensity in combination with optimal imaging and nearly optimal pump pulse duration I have demonstrated the highest pulse energies up to 0.4 mJ in the frequency range below 1

THz. I have demonstrated a generation efficiency of 0.77% which is the highest for large pulse energies. [S2]

Thesis statment 4 I have demonstrated for the first time generation of THz pulses with parameters that are applicable for charged-particle acceleration, for example for THz driven evanescent-wave proton post-accelerator. In this lithium niobate based cryogenic-cooled THz source I have measured in-focus waveforms that show a spectral peak at about 0.2 THz and a 0.65 MV/cm calculated peak electric field strength. [S2]

Thesis statment 5 I have investigated experimentally near-field THz beam profiles. Measurements showed that increasing the pump fluence leads to a beam diameter decrease in the dispersion plane while there is no change in the plane vertical to it. Moreover, performing the corresponding measurements for THz beam divergence I have found that the angle increases in the horizontal direction while no significant change can be observed in the vertical direction [S3]. These results indicate that nonlinear beam distortions have a high relevance at designing high energy THz sources.

9. fejezet

Magyar nyelvű összefoglaló

9.1. Előzmények és célkitűzés

Az utóbbi évtizedekben kifejlesztett nagyintenzitású, egyciklusú terahertzes (THz) forrásoknak köszönhetően új kutatási területek is megjelentek. A fejlődésnek köszönhetően olyan alkalmazások váltak elérhetővé, mint a THz sugárzással segített attoszekundumos impulzusok keltése [9], THz pumpa – THz próba mérések [6], molekulaorientációs kísérletek intenzív terekben [7]. A jelenleg még nem előállítható, nagy térerősséggel rendelkező források további felhasználási területek elterjedését tennék lehetővé, mint a relativisztikus elektroncsomók gyorsítása és manipulálása [10-12], lézerrel keltett protonok és ionok utógyorsítása [13], és egylövéses multispektrális képalkotás.

Napjainkban a nagy térerősségű terahertzes források a MV/cm tartományban csak magasabb frekvenciákon érhetőek el [14]. Félvezető [14] és organikus kristály alapú terahertzes források [21,22,72] a magas nemlineáris együtthatójuknak köszönhetően jó keltési hatásfokkal rendelkeznek, azonban csak magasabb frekvenciákon működnek (1 THz – 10 THz). Ebből adódóan a keltett nyaláb jól fókuszálható és nagy térerősségeket lehet elérni. Habár az alacsonyabb frekvenciákon (0.1 THz – 2 THz) működő források előnyösebbnek mutatkoznak az említett kutatási területek számára – mivel a

hosszabb hullámhossz jobban illeszkedik a részecskesugarak transzverzális méretéhez -, ezen forrásokkal keltett impulzusenergiák és térerősségek még nem elegendőek. A cink-tellurid (ZnTe) alapú források jó tulajdonságokkal rendelkeznek, nagy terahertz energia azonban csak a háromfotonos abszorpciós limit feletti pumpálás esetén érhető el [46]. Döntött impulzusfrontú elrendezésben [1] hűtött lítium-niobát ($LiNbO_3$, LN) oxidkristályt használva jó keltési hatásfok érhető el, mely alapján nagy terahertz energiák érhetők el a 0.1 THz - 1 THz frekvenciatartományon.

Ezért célom, hogy optimalizáljam a lítium-niobátban femtoszekundumos lézerimpulzusok optikai egyenirányításával döntött impulzusfrontú elrendezésben keltett terahertzes forrásokat [1]. Elméleti számolások alapján konverziós hatásfok növekedés várható optimális pumpáló impulzushosszak és a LN forrás kristály kriogenikus hűtése esetén [15-17]. Az elméleti eredmények bizonyításául kísérleteket végeztem döntött impulzusfrontú terahertzes forrásokon különböző elrendezések segítségével, több különböző pumpáló impulzushosszat, kristályhőmérsékletet és leképezési konfigurációt használva.

9.2. Módszerek

Az elméleti eredményeket [14] melyek megjósolták, hogy az egyciklusú terahertzes impulzusok konverziós hatásfoka növelhető, a következő kísérletek elvégzésével bizonyítottam:

(i) vizsgáltam lítium-niobát alapú terahertzes forrásokat olyan elrendezésben, ahol a forrás kristály 0.39 ps és és 0.65 ps közötti transzformáció-limitált impulzusokkal volt megvilágítva, összesen 15 mJ impulzusenergiával, 1030 nm központi hullámhosszal, és meghatároztam a hatékony THz keltéshez szükséges optimális pumpáló impulzushosszat.

(ii) vizsgáltam kriogenikus hőmérsékletre hűtött lítium-niobát alapú terahertzes for-

rásokat és kiszámoltam a két hőmérsékleten mért hatásfok arányát (η_{CT}/η_{RT}) közepes (45 μJ) és nagy (50-180 μJ) terahertzes impulzusenergiákra.

(iii) terahertzes hullámformákat mértem elektro-optikai mintavételezéssel, az elérhető legnagyobb impulzusenergiákon, alacsony frekvenciatartomány esetén.

A továbbiakban összehasonlítottam két terahertzes forrást, melyek optimális leképezési paraméterek alapján voltak felépítve. A kísérlet során alacsony terahertzes frekvenciájú, döntött impulzusfrontú elrendezésben felépített forrásokról hasznos információkhoz jutottunk.

Az első elrendezés esetében kétlencsés leképezést, míg a második esetben egylencsés leképezést építettem fel. Megvalósítottam az elrendezések térbeli karakterizálását lehetővé tevő elrendezést és a forrásokhoz kapcsolódó elektro-optikai elrendezést, hogy nyalábdivergencia és foltméret ellipticitás-változást tudjak vizsgálni különböző pumpáló intenzitások esetén. Ezen információk kiemelt fontosságúak nyalábfókuszálást és nyalábterjedést érintő tervezésekkor.

9.3. Eredmények

1. tézispont Kriogenikus hőmérsékletre hűtött lítium-niobátban történő, ultrarövid impulzusok optikai egyenirányításán alapuló THz-es forrást vizsgáltam annak érdekében, hogy növeljem a pumpa – THz energia konverziós hatásfokát különböző hosszúságú transzformáció limitált impulzusok segítségével. Megmutattam, hogy az elméleti számolásokkal összhangban, a hosszabb impulzusok segítségével nagyobb konverziós hatásfok érhető el [S1]. Ezenkívül kísérletileg is bizonyítottam, hogy rövidebb impulzusok használatával nagyobb terahertzbeli sávszélesség érhető el.

2. tézispont Döntött impulzusfronton alapuló, kriogenikus hőmérsékletre hűtött lítium-niobátban történő THz keltés hatásfokát vizsgáltam különböző elrendezésekben. Megmutattam, hogy hűtés hatására a konverziós hatásfok a szobahőmérsékleti hatásfokhoz képest akár négyszeres is lehet 45μJ THz impulzusenergiáig, míg 50μJ és 180μJ impulzusenergia között 2.4-szeres javulást sikerült elérni. [S1, S2]

3. tézispont Döntött impulzusfronton alapuló, szobahőmérsékletű lítium-niobát kristályt megvilágítva nagyenergiájú és nagy intenzitású pumpáló lézerrel, optimális leképezést és közel optimális impulzushosszt használva megmutattam, hogy a keltési hatásfok 0.77% is lehet, elérve a 0.4 mJ impulzusenergiát, ami adott frekvenciatartományban az elért legnagyobbnak számít. [S2]

4. tézispont Elsőként keltettem terahertzes impulzusokat olyan paraméterekkel, amelyek megfelelőnek bizonyulnak töltött részecskék gyorsítására, mint például evaneszcens terahertzes hullámokkal történő proton utógyorsításra. Lítium-niobát alapú, kriogenikus hőmérsékletre hűtött terahertzes forrás segítségével lefókuszált hullámformákat mértem 0.2 THz spektrális csúccsal és 0.65 MV/cm számolt csúcstérerősséggel. [S2]

5. tézispont Kísérletileg megvizsgáltam THz-es források közeltérbeli nyalábképét. Méréseim alapján elmondható, hogy a pumpáló intenzitás növelésével a terahertzes nyaláb diszperzió síkjába eső mérete csökken, az erre merőlegesirányú síkban azonban nem tapasztalható változás. Folytatva a vizsgálatokat megmutattam, hogy a horizontális irányban a nyaláb divergenciaszöge növekszik, míg a vertikális irányban ismét nincs számottevő változás [S3]. Eredményeim megmutatták, hogy nagyenergiájú források és hozzájuk kapcsolódó elrendezések tervezésénél elengedhetetlen a nemlineáris nyalábváltozások figyelembevétele.

Publications

10.1 Referred articles supporting the thesis points

[S1] C Vicario, B Monoszlai, Cs Lombosi, A Mareczko, A Courjaud, JA Fülöp, CP Hauri, *"Pump pulse width and temperature effects in lithium niobate for efficient THz generation"* Optics Letters **38** (24), 5373-5376

[S2] JA Fülöp, Z Ollmann, Cs Lombosi, Ch Skrobol, S Klingebiel, L Pálfalvi, F Krausz, S K, J Hebling, *"Efficient generation of THz pulses with 0.4 mJ energy"*, Optics Express **22** (17), 20155-20163

[S3] C Lombosi, G Polónyi, M Mechler, Z Ollmann, J Hebling, JA Fülöp, *"Nonlinear distortion of intense THz beams"*, New Journal of Physics **17** (8), 083041

10.2 Other publications

[S4] W.Schneider, A Ryabov, Cs Lombosi, T Metzger, Zs Major, JA Fülöp, Peter Baum, *"800-fs, 330-μJ pulses from a 100-W regenerative Yb: YAG thin-disk amplifier at 300 kHz and THz generation in $LiNbO_3$"*, Optics Letters **39** (23), 6604-6607

List of Figures

Acknowledgements

I would like to thank my supervisors, József Fülöp and János Hebling for their guidance throughout my years at the High-field THz Research Group. Without their professional support this work could not have been completed.

I would like to thank Balázs Monoszlai, Zoltán Ollmann, and Gábor Almási for sharing their experience and knowledge about physics and scientific life; Zoltán Tibai and Andrea Lóki for personal encouragement; and Mátyás Mechler for carefully reading the manuscript and adding their indispensable comments and suggestions to it. I would also like to express my gratitude towards every colleague of Institute of Physics for creating a friendly and supportive workspace, and for many interesting and excited discussions about various subjects.

Last, but not least, I would like to thank my family, and my friends for believing in me, encouraging me and providing their plentiful support.

References

[1] J. Hebling, G. Almási, I. Z. Kozma, and J. Kuhl, Opt. Express **10**, 1161 (2002).

[2] J. A. Fülöp, L. Pálfalvi, S. Klingebiel, G. Almási, F. Krausz, S. Karsch, and J. Hebling, Opt. Lett. **37**, 557 (2012).

[3] K. L. Yeh, M. C. Hoffmann, J. Hebling, and K. A. Nelson, Applied Physics Letters **90**, 171121 (2007).

[4] J. Hebling, K.-L. Yeh, M. C. Hoffmann, B. Bartal, and K. A. Nelson, J. Opt. Soc. Am. B **25**, B6 (2008).

[5] A. G. Stepanov, L. Bonacina, S. V. Chekalin, and J.-P. Wolf, Opt. Lett. **33**, 2497 (2008).

[6] J. Hebling, M. C. Hoffmann, H. Y. Hwang, K.-L. Yeh, and K. A. Nelson, Physical Review B **81**, 035201 (2010).

[7] S. Fleischer, Y. Zhou, R. W. Field, and K. A. Nelson, Physical Review Letters **107**, 163603 (2011).

[8] B. Schütte, U. Frühling, M. Wieland, A. Azima, and M. Drescher, Opt. Express **19**, 18833 (2011).

[9] E. Balogh, K. Kovacs, P. Dombi, J. A. Fulop, G. Farkas, J. Hebling, V. Tosa, and K. Varju, Physical Review A **84**, 023806 (2011).

[10] J. Hebling, J. A. Fülöp, M. I. Mechler, L. Pálfalvi, C. Töke, and G. Almási, arxiv.org (2011).

[11] L. J. Wong, A. Fallahi, and F. X. Kärtner, Opt. Express **21**, 9792 (2013).

[12] Z. Tibai, L. Pálfalvi, J. A. Fülöp, G. Almási, and J. Hebling, in *4th EOS Topical Meeting on Terahertz Science and Technology* Camogli, Italy, 2014).

[13] L. Pálfalvi, J. A. Fülöp, G. Tóth, and J. Hebling, Physical Review Special Topics - Accelerators and Beams **17**, 031301 (2014).

[14] A. Sell, A. Leitenstorfer, and R. Huber, Opt. Lett. **33**, 2767 (2008).

[15] J. A. Fülöp, L. Pálfalvi, G. Almási, and J. Hebling, Opt. Express **18**, 12311 (2010).

[16] J. A. Fülöp, L. Pálfalvi, M. C. Hoffmann, and J. Hebling, Opt. Express **19**, 15090 (2011).

[17] M. I. Bakunov, S. B. Bodrov, and E. A. Mashkovich, J. Opt. Soc. Am. B **28**, 1724 (2011).

[18] J. R. S. Morris, Y. R., Optics Communications 3, **81** (1971).

[19] K. H. Yang, P. L. Richards, and Y. R. Shen, Applied Physics Letters **19**, 320 (1971).

[20] D. H. Auston, K. P. Cheung, J. A. Valdmanis, and D. A. Kleinman, Physical Review Letters **53**, 1555 (1984).

[21] C. P. Hauri, C. Ruchert, C. Vicario, and F. Ardana, Applied Physics Letters **99**, 161116 (2011).

[22] A. Schneider, M. Neis, M. Stillhart, B. Ruiz, R. U. A. Khan, and P. Günter, J. Opt. Soc. Am. B **23**, 1822 (2006).

[23] C. Vicario, A. V. Ovchinnikov, S. I. Ashitkov, M. B. Agranat, V. E. Fortov, and C. P. Hauri, Opt. Lett. **39**, 6632 (2014).

[24] M. Shalaby and C. P. Hauri, **6**, 5976 (2015).

[25] P. A. Franken, A. E. Hill, C. W. Peters, and G. Weinreich, Physical Review Letters **7**, 118 (1961).

[26] A. W. Smith and N. Braslau, Journal of Applied Physics **34**, 2105 (1963).

[27] M. Bass, P. A. Franken, A. E. Hill, C. W. Peters, and G. Weinreich, Physical Review Letters 8, **18** (1962).

[28] R. W. Terhune, P. D. Maker, and C. M. Savage, Physical Review Letters **8**, 404 (1962).

[29] M. Bass, P. A. Franken, J. F. Ward, and G. Weinreich, Physical Review Letters **9**, 446 (1962).

[30] R. W. Boyd, *Nonlinear optics* (2008).

[31] G. New, *Introduction to nonlinear optics* (Cambridge University Press, 2011).

[32] G. Brooker, *Modern classical optics* (Oxford University Press, 2003).

[33] M. Born and E. Wolf, *Principles of optics* (Cambridge University Press, 1999).

[34] J.-C. Diels and W. Rudolph, *Ultrashort laser pulse phenomena* (Academic Press, 1996).

[35] Y.-S. Lee, *Principles of Terahertz Science and Technology* (Springer US, 2009).

[36] C. Ruchert, C. Vicario, and C. P. Hauri, Opt. Lett. **37**, 899 (2012).

[37] K. L. Vodopyanov and L. A. Kulevskii, Optics Communications **118**, 375 (1995).

[38] N. Piccioli, R. Le Toullec, M. Mejatty, and M. Balkanski, Appl. Opt. **16**, 1236 (1977).

[39] D. F. Edwards, in *Handbook of Optical Constants of Solids* (Academic Press, Burlington, 1997), pp. 473.

[40] K. Sato and S. Adachi, Journal of Applied Physics **73**, 926 (1993).

[41] M. Schall, M. Walther, and P. Uhd Jepsen, Physical Review B **64**, 094301 (2001).

[42] D. H. Jundt, M. M. Fejer, and R. L. Byer, IEEE Journal of Quantum Electronics **26**, 135 (1990).

[43] M. Schall, H. Helm, and S. R. Keiding, International Journal of Infrared and Millimeter Waves **20**, 595 (1999).

[44] J. Hebling, A. G. Stepanov, G. Almási, B. Bartal, and J. Kuhl, Applied Physics B **78**, 593 (2004).

[45] F. Blanchard *et al.*, Opt. Express **15**, 13212 (2007).

[46] G. Polónyi *et al.*, Opt. Express **24**, 23872 (2016).

[47] E. D. Palik, in *Handbook of Optical Constants of Solids* (Academic Press, Burlington, 1997), pp. 695.

[48] D. H. Auston and P. R. Smith, Applied Physics Letters **43**, 631 (1983).

[49] M. Theuer, G. Torosyan, C. Rau, R. Beigang, K. Maki, C. Otani, and K. Kawase, Applied Physics Letters **88**, 071122 (2006).

[50] S. B. Bodrov, A. N. Stepanov, M. I. Bakunov, B. V. Shishkin, I. E. Ilyakov, and R. A. Akhmedzhanov, Opt. Express **17**, 1871 (2009).

[51] J. A. Armstrong, N. Bloembergen, J. Ducuing, and P. S. Pershan, Physical Review **127**, 1918 (1962).

[52] G. D. Boyd, A. Ashkin, J. M. Dziedzic, and D. A. Kleinman, Physical Review **137**, A1305 (1965).

[53] Y. S. Lee, T. Meade, V. Perlin, H. Winful, T. B. Norris, and A. Galvanauskas, Applied Physics Letters **76**, 2505 (2000).

[54] Y. S. Lee, T. Meade, M. DeCamp, T. B. Norris, and A. Galvanauskas, Applied Physics Letters **77**, 1244 (2000).

[55] Y. S. Lee, T. Meade, T. B. Norris, and A. Galvanauskas, Applied Physics Letters **78**, 3583 (2001).

[56] P. L. Richards, Journal of Applied Physics **76**, 1 (1994).

[57] S. P. Langley, Nature **25** (1881).

[58] W. S. Boyle and K. F. Rodgers, J. Opt. Soc. Am. **49**, 66 (1959).

[59] H. P. Beerman, IEEE Transactions on Electron Devices **16**, 554 (1969).

[60] N. Oda, in *Comptes Rendus Physique* (2010), pp. 496.

[61] P. R. Smith, D. H. Auston, and M. C. Nuss, IEEE Journal of Quantum Electronics **24**, 255 (1988).

[62] S. E. Ralph and D. Grischkowsky, Applied Physics Letters **60**, 1070 (1992).

[63] S. Kono, M. Tani, P. Gu, and K. Sakai, Applied Physics Letters **77**, 4104 (2000).

[64] W. Qi and Z. Xi-Cheng, IEEE Journal of Selected Topics in Quantum Electronics **2**, 693 (1996).

[65] I. H. Stefan Gorenflo, Armin Lambrecht, Bernd Fischer, Matthias Hoffmann, Hanspeter Helm, Peter Uhd Jepsen, Technisches Messen **72**, 427 (2009).

[66] P. C. M. Planken, H.-K. Nienhuys, H. J. Bakker, and T. Wenckebach, J. Opt. Soc. Am. B **18**, 313 (2001).

[67] T. Volk, N. Rubinina, and M. Wöhlecke, J. Opt. Soc. Am. B **11**, 1681 (1994).

[68] L. Pálfalvi, J. Hebling, G. Almási, Á. Péter, K. Polgár, K. Lengyel, and R. Szipöcs, Journal of Applied Physics **95**, 902 (2004).

[69] K. Lengyel *et al.*, Applied Physics Reviews **2**, 040601 (2015).

[70] L. Pálfalvi, J. Hebling, J. Kuhl, Á. Péter, and K. Polgár, Journal of Applied Physics **97**, 123505 (2005).

[71] S.-W. Huang, E. Granados, W. R. Huang, K.-H. Hong, L. E. Zapata, and F. X. Kärtner, Opt. Lett. **38**, 796 (2013).

[72] C. Vicario, B. Monoszlai, and C. P. Hauri, Physical Review Letters **112**, 213901 (2014).

[73] Y. Yang, D. Shutler A Fau - Grischkowsky, and D. Grischkowsky.

[74] A. Riefer, S. Sanna, A. Schindlmayr, and W. G. Schmidt, Physical Review B **87**, 195208 (2013).

[75] S. Klingebiel, C. Wandt, C. Skrobol, I. Ahmad, S. A. Trushin, Z. Major, F. Krausz, and S. Karsch, Opt. Express **19**, 5357 (2011).

[76] Y. Shen, T. Watanabe, D. A. Arena, C. C. Kao, J. B. Murphy, T. Y. Tsang, X. J. Wang, and G. L. Carr, Physical Review Letters **99**, 043901 (2007).

[77] C. Vicario, B. Monoszlai, C. Lombosi, A. Mareczko, A. Courjaud, J. A. Fülöp, and C. P. Hauri, Opt. Lett. **38**, 5373 (2013).

[78] H. Hirori, A. Doi, F. Blanchard, and K. Tanaka, Applied Physics Letters **98**, 091106 (2011).

[79] A. Sharma, Z. Tibai, and J. Hebling, Physics of Plasmas **23**, 063111 (2016).

[80] L. Tokodi, J. Hebling, and L. Pálfalvi, Journal of Infrared, Millimeter, and Terahertz Waves **38**, 22 (2017).

[81] S. A. Ku, C. M. Tu, W. C. Chu, C. W. Luo, K. H. Wu, A. Yabushita, C. C. Chi, and T. Kobayashi, Opt. Express **21**, 13930 (2013).

[82] S. B. Bodrov, A. A. Murzanev, Y. A. Sergeev, Y. A. Malkov, and A. N. Stepanov, Applied Physics Letters **103**, 251103 (2013).

[83] K. Ravi, W. R. Huang, S. Carbajo, X. Wu, and F. Kärtner, Opt. Express **22**, 20239 (2014).

[84] M. T. Reiten, S. A. Harmon, and R. A. Cheville, J. Opt. Soc. Am. B **20**, 2215 (2003).

[85] J. F. Molloy, M. Naftaly, and R. A. Dudley, IEEE Journal of Selected Topics in Quantum Electronics **19**, 8401508 (2013).

[86] T. I. Oh, Y. J. Yoo, Y. S. You, and K. Y. Kim, Applied Physics Letters **105**, 041103 (2014).

[87] P. Klarskov, A. C. Strikwerda, K. Iwaszczuk, and P. U. Jepsen, New Journal of Physics **15**, 075012 (2013).

[88] P. Klarskov, A. C. Strikwerda, T. Wang, M. Zalkovskij, and P. U. Jepsen, Proc. SPIE 8624, Terahertz, RF, Millimeter, and Submillimeter-Wave Technology and Applications VI **149**, 05011 (2013).

[89] T. Hattori and K. Takeuchi, Opt. Express **15**, 8076 (2007).

[90] M. Jewariya, M. Nagai, and K. Tanaka, J. Opt. Soc. Am. B **26**, A101 (2009).